Check for updates

JGR Atmospheres

RESEARCH ARTICLE
10.1029/2024JD043236

Ice-Nucleating Particle and Cloud Ice Crystal Concentrations Associated With Developing Summertime Deep Convective Clouds in South-Western USA

Martin I. Daily[1], Joseph Robinson[1], Declan L. Finney[1,2], Erin N. Raif[1], James B. McQuaid[1], Alberto Sanchez-Marroquin[3], Kezhen Hu[4], Gary Lloyd[4], Michael Flynn[4], Paul R. Field[1,5], Keith N. Bower[4], Hugh Coe[4], Martin W. Gallagher[4], Alan M. Blyth[1,2], and Benjamin J. Murray[1]

[1]Insititute for Climate and Atmospheric Science, University of Leeds, Leeds, UK, [2]National Centre for Atmospheric Science, University of Leeds, Leeds, UK, [3]Barcelona Supercomputing Centre, Barcelona, Spain, [4]Centre for Atmospheric Science, University of Manchester, Manchester, UK, [5]The Met Office, Exeter, UK

Key Points:

- Ice-nucleating particles (INP) were measured during an aircraft campaign targeting deep convective clouds in New Mexico, USA
- Consistently high INP concentrations extended from near surface to 5 km altitude, possibly associated with fertile soil dust
- The concentrations of the first observed ice particles measured within growing convective clouds were consistent with the measured INP spectra

Supporting Information:

Supporting Information may be found in the online version of this article.

Correspondence to:

M. I. Daily,
m.i.daily@leeds.ac.uk

Citation:

Daily, M. I., Robinson, J., Finney, D. L., Raif, E. N., McQuaid, J. B., Sanchez-Marroquin, A., et al. (2026). Ice-nucleating particle and cloud ice crystal concentrations associated with developing summertime deep convective clouds in south-western USA. *Journal of Geophysical Research: Atmospheres*, *131*, e2024JD043236. https://doi.org/10.1029/2024JD043236

Received 15 JAN 2025
Accepted 20 JAN 2026

Author Contributions:

Conceptualization: Martin I. Daily, Declan L. Finney, Gary Lloyd, Paul R. Field, Alan M. Blyth, Benjamin J. Murray
Data curation: Martin I. Daily, Joseph Robinson, Gary Lloyd, Michael Flynn
Formal analysis: Martin I. Daily, Erin N. Raif, Kezhen Hu, Gary Lloyd, Alan M. Blyth

© 2026. The Author(s).
This is an open access article under the terms of the Creative Commons Attribution License, which permits use, distribution and reproduction in any medium, provided the original work is properly cited.

Abstract Ice-nucleating particles (INPs), essential for initiating primary ice production in many mixed-phase clouds, have only rarely been measured in air directly relevant for deep convective clouds. In July–August 2022 we used an aircraft to sample aerosol near developing deep convective clouds over Magdalena Mountain, New Mexico, USA. We observed INP concentrations consistently at the upper end of those typically observed in continental air with ∼0.01–0.5 L^{-1} at −8°C. Vertically resolved sampling revealed a deep aerosol layer extending 3–4 km above ground level, in which INP concentrations only varied within an order of magnitude. Above this layer, low temperature INP (<−15°C) decreased, but high temperature INP (>−15°C) remained abundant, despite having been collected in air with a lower aerosol concentration. Compositional analysis of filter aerosol showed mineral dusts dominated the surface area of aerosol larger than ∼800 nm, but the activity of the mineral alone cannot account for the observed INP concentrations. We suggest that these mineral dust particles are internally mixed with ice-nucleating biogenic components, as they would be in organic containing fertile soils, or there is an additional biogenic/biological ice-nucleating component(s) strongly enhancing the INP population over what would be expected for mineral dust alone. Finally, ice particle measurements in rising cloud turrets at progressively colder temperatures reveal that the temperature at which we first observed ice was consistent with the measured INP spectra.

Plain Language Summary Ice-nucleating particles (INPs) are rare aerosol particles that trigger formation of ice crystals in clouds and are thought to play an important role in how much incoming solar radiation gets reflected off the tops of thunderstorms back into space. However, a lack of field measurements limits our understanding of ice production in cloud and how this relates to aerosol particles. During July–August 2022 an aircraft was used to collect aerosol on filters and measure the abundance and composition of airborne INPs, along with the concentration of ice whilst flying in and around growing storm clouds over New Mexico, USA. INP concentrations were measured outside of storm clouds at several different heights. Analysis of the filters suggested the particles acting as INPs are mineral dust particles mixed with some biological matter, perhaps originating from fertile soil. When the aircraft flew through the tops of growing clouds we found that the temperature at which ice was first observed was consistent with the INP measurements. The data collected here will help improve our understanding of deep convective clouds, leading to their improved simulation in models.

1. Introduction

The equilibrium climate sensitivity (i.e., the global mean surface temperature change resulting from a doubling of carbon dioxide mixing ratio) remains uncertain in part due to divergent cloud feedbacks partly stemming from a lack of understanding of cloud microphysical processes (Ceppi et al., 2017; Sherwood et al., 2020). Deep convective clouds produce high cloud anvils leading to radiative feedbacks depending on parameters such as their albedo, areal extent and lifetime. These parameters can depend on the microphysical processes, including ice production, occurring in the mixed-phase regime (Bony et al., 2016; Hartmann et al., 2018), yet uncertainties in how to represent them contributes to significant spread in feedbacks produced by global circulation models (Gettelman & Sherwood, 2016). Ice production in clouds strongly controls rain initiation (McFarquhar et al., 2017) and their radiative properties (Boucher et al., 2014; Hawker, Miltenberger, Johnson, et al., 2021;

21698996, 2026, 3, Downloaded from https://agupubs.onlinelibrary.wiley.com/doi/10.1029/2024JD043236 by University Of Leeds The Brotherton Library, Wiley Online Library on [11/02/2026]. See the Terms and Conditions (https://onlinelibrary.wiley.com/terms-and-conditions) on Wiley Online Library for rules of use; OA articles are governed by the applicable Creative Commons License

Funding acquisition: Paul R. Field, Keith N. Bower, Hugh Coe, Martin W. Gallagher, Alan M. Blyth, Benjamin J. Murray
Investigation: Martin I. Daily, Joseph Robinson, James B. McQuaid, Alberto Sanchez-Marroquin, Kezhen Hu, Gary Lloyd, Michael Flynn, Paul R. Field, Keith N. Bower, Hugh Coe, Martin W. Gallagher, Alan M. Blyth, Benjamin J. Murray
Methodology: Martin I. Daily, Declan L. Finney, Erin N. Raif, Alberto Sanchez-Marroquin, Gary Lloyd, Paul R. Field, Keith N. Bower, Hugh Coe, Martin W. Gallagher, Alan M. Blyth, Benjamin J. Murray
Project administration: Martin I. Daily, Declan L. Finney, Alan M. Blyth, Benjamin J. Murray
Resources: Gary Lloyd, Michael Flynn, Alan M. Blyth, Benjamin J. Murray
Software: Martin I. Daily, Erin N. Raif, Gary Lloyd
Supervision: James B. McQuaid, Paul R. Field, Keith N. Bower, Hugh Coe, Martin W. Gallagher, Alan M. Blyth, Benjamin J. Murray
Validation: Declan L. Finney
Visualization: Martin I. Daily
Writing – original draft: Martin I. Daily
Writing – review & editing: Martin I. Daily, Declan L. Finney, James B. McQuaid, Gary Lloyd, Paul R. Field, Martin W. Gallagher, Alan M. Blyth, Benjamin J. Murray

Hawker, Miltenberger, Wilkinson, et al., 2021). At temperatures above about −35°C cloud ice production must be initiated by the presence of ice-nucleating particles (INPs) (Herbert et al., 2015; Ickes et al., 2015). INPs are the subset of aerosol particles that can initiate heterogeneous ice nucleation in supercooled cloud droplets via immersion, contact, or deposition modes (Vali et al., 2015), with immersion considered most crucial in the liquid water-saturated mixed-phase regime (Ansmann et al., 2008; Field et al., 2012; Murray et al., 2012).

Modeling studies have underscored a sensitivity of ice production to INP population, thereby affecting anvil properties in deep convective clouds (Deng et al., 2018; Fan et al., 2010, 2017; Gibbons et al., 2018). The choice of INP parameterization used, which may be prognostic based on aerosol content (DeMott et al., 2010, 2015; Harrison et al., 2019) or simply temperature dependent (Cooper, 1986; Meyers et al., 1992), has a strong influence on these modeled deep convective clouds (Hawker, Miltenberger, Johnson, et al., 2021; Hawker, Miltenberger, Wilkinson, et al., 2021).

Understanding of the sources and transport of atmospheric INP is, therefore, crucial for accurate representation in models (Kanji et al., 2017). Various aerosol types serve as INP including silicate mineral dust, controlled by the K-feldspar component (Atkinson et al., 2013; Boose et al., 2016; Harrison et al., 2016), which tends to dominate INP concentration at temperatures below about −20°C, while biogenic INP types, such as proteinaceous material from bacteria and fungi, contribute to INP activity up to about −3°C (Conen & Yakutin, 2018; Hill et al., 2014; Huang et al., 2021; O'Sullivan et al., 2015, 2016). Non-proteinaceous biogenic material, including pollen-derived macromolecules (Dreischmeier et al., 2017; Murray et al., 2022; Pummer et al., 2012) and the plant structure-building compounds lignin and cellulose (Bogler & Borduas-Dedekind, 2020; Hiranuma et al., 2019) are also important INP types, potentially competing with dust (Hader et al., 2014). The proteinaceous component of INPs could originate from Primary Biological Aerosol Particles (PBAPs) such as fungal spores (Beall et al., 2021; Morris et al., 2013; Spracklen & Heald, 2014), pollen particles (Matthews et al., 2023; Pummer et al., 2012) and bacteria (Cochet & Widehem, 2000; Maki et al., 1974) or alternatively fertile soil dust internally mixed with ice-nucleating macromolecules or other ice nucleating detritus from life (Conen et al., 2011; McCluskey et al., 2018; O'Sullivan et al., 2014, 2016). Sea spray derived aerosols composed of internal mixtures of sea salt and organic matter (McCluskey et al., 2018; Wilson et al., 2015) are another INP category, which although generally less potent than mineral dust, may dominate INP contributions at remote oceanic and coastal settings (Herbert et al., 2025; Vergara-Temprado et al., 2017).

Numerous INP sampling campaigns worldwide support our understanding of which INP types are important where, and indicate what the dominant sources of INP are (Kanji et al., 2017), although most are ground-based observations, which may be disproportionally influenced by surface INP sources in the immediate vicinity. Airborne INP sampling can address this by directly sampling INP populations in air that enters and influences specific clouds, as well as by delineating the vertical distribution of INPs in the atmosphere. The vertical profile of INPs may matter for the development of deep convective clouds, since it has been shown in a modeling study of shallow cumulus that about 70% of aerosol were ingested at cloud base, while the remainder were laterally entrained (Hoffmann et al., 2015). This underlines the importance of understanding the 3-dimensional distribution of INPs when attempting to model deep convective cloud development, which may be influenced by both boundary layer air and entrained air at higher altitudes. Previous airborne campaigns have shown varying trends of vertical INP distribution, with examples recorded of both decreasing INP (Brasseur et al., 2024; Patade et al., 2014; Schnell, 1982; Wu et al., 2022) and increasing (He et al., 2023; Knopf et al., 2023; Levin et al., 2019; Moore et al., 2024) with altitude. In addition to spatial distribution, compositional data can allow targeted investigation of specific INP populations such as desert dust (Patnaude et al., 2025; Price et al., 2018), wildfire smoke (Barry et al., 2021), PBAPs (Sanchez-Marroquin et al., 2021) and volcanic ash (Sanchez-Marroquin et al., 2020). This can ultimately provide insights into long-range transport of INPs, where for example, airborne dust containing biogenic INP originating from Asia was sampled at several kilometers of altitude during flights above California (Creamean et al., 2013).

Aircraft campaigns also present the opportunity to directly compare INP concentrations with cloud microphysics data such as ice particle number concentration (N_{ice}). Past studies find N_{ice} in clouds can greatly exceed measured INP concentrations (Hobbs & Rangno, 1985) or predicted INP concentrations (Cantrell & Heymsfield, 2005; Field et al., 2017; Mossop & Ono, 1969). This forms the basis for the existence of secondary ice production (SIP) processes that serve to multiply ice particle concentrations through a range of potential mechanisms (Field et al., 2017; Korolev & Leisner, 2020). Quantifying SIP requires knowledge of the concentration of primary ice

21698996, 2026, 3, Downloaded from https://agupubs.onlinelibrary.wiley.com/doi/10.1029/2024JD043236 by University Of Leeds The Brotherton Library, Wiley Online Library on [11/02/2026]. See the Terms and Conditions (https://onlinelibrary.wiley.com/terms-and-conditions) on Wiley Online Library for rules of use; OA articles are governed by the applicable Creative Commons License

crystals, which should be linked to the INP concentration (or primary ice production) (Cooper, 1986; Lloyd et al., 2020; Taylor et al., 2016). However, generally there has been, to date, a dearth of airborne deep convective cloud microphysical and aerosol observations with large data sets of simultaneous measurements of N_{ice} and INPs. A recent campaign focused on cumulus clouds is reported in Lawson et al. (2023), where airborne measurement were conducted over wide area of the Great Plains region of the central United States in 2021. They find that first ice was typically detected below around −10°C, which is consistent with their INP measurements. Campaigns flown around tropical maritime convection found N_{ice} present warmer than −8°C at concentrations much greater than observed INPs (Lloyd et al., 2020; Yang et al., 2020) (Price et al. [2018] report INP spectra for the campaign discussed by Lloyd et al. (2020)).

Here we present airborne INP measurements from the DCMEX (Deep Convective Microphysics EXperiment) measurement campaign, which took place in New Mexico during July–August 2022 and included coordinated aircraft and ground-based radar observations, targeting deep convective clouds that formed almost daily over the Magdalena Mountains, west of Socorro, New Mexico, USA, during the project. A full description of the campaign and measurements made during the flights is available (Finney et al., 2024). The "laboratory-like" clouds that can frequently form at the Magdalena Mountains during the summer monsoon period enabled extensive measurements of INP and N_{ice} at the same location, also allowing for variations in aerosol concentration, meteorology, sampled air mass, and vertical mixing state to be assessed. The campaign builds on a cloud microphysics-only airborne study at this location in 1987 where measurements of primary N_{ice} were made but no INP measurements were made (Blyth & Latham, 1993). Then, it was found that the first detectable primary N_{ice} observed in growing clouds at about −10°C was at higher temperatures than expected INP according to the Fletcher INP parameterization available at the time (Fletcher et al., 1962). For this study, the INP data presented here were collected contemporaneously with ice particle number data, providing an opportunity to directly compare them and investigate, for example, secondary ice-production processes in future studies.

2. Methods

2.1. Aerosol Sampling and Cloud Microphysics Measurements From an Aircraft

During the DCMEX campaign conducted in July–August 2022, aerosol sampling was conducted using filters via the UK's Facility for Airborne Atmospheric Measurement (FAAM) BAe-146-301 atmospheric research aircraft. The campaign focused on an area approximately 75 km by 75 km, around the Magdalena Mountains (33.97°N, 107.18°W), situated roughly 20 km west of Socorro, New Mexico, where convective clouds "anchored" to mountains are common during the summer monsoon (Figure 1). The Langmuir Laboratory for Atmospheric Research, operated by New Mexico Tech and located at the summit of the Magdalena Mountains, functioned as the geographical focus of the flights and as the base for ground-based observations during the wider DCMEX campaign. The objective of the 19 flights (C297–C315) was to transit from our base at Albuquerque International Airport and arrive at Magdalena Mountains in late morning before any convective activity began. Here, we conducted clear-air aerosol sampling runs along a fixed circuit around waypoints DC1–DC4 (Figure 1a), above the mountain's base, approximately 1.5–2.0 km ASL (above sea level) at the lowest and highest points of the circuit respectively. Subsequently, microphysics sampling passes were conducted in developing clouds. Most filter samples were collected before deep convective clouds initiated over the mountain, with exceptions for cases where cloud pass microphysics sampling took precedence.

Each flight typically included up to four filter sampling runs, usually comprising a single lap of the aerosol circuit (see Figure 1a; approximately 120 km, taking 20 min) and at various altitudes ranging from low-level, terrain-following runs (100–300 m above surface) to higher altitude, less surface-influenced, runs at a maximum altitude of 7,300 m. This approach facilitated vertical delineation of INP concentrations through repeated airborne sampling at a fixed location.

Real-time aerosol sizing data informed the estimation of the planetary boundary layer depth during flights, guiding sampling strategy. Aerosol particle size distribution data were collected during flights using the FAAM aircraft's underwing optical particle counters: the Passive Cavity Aerosol Spectrometer Probe 100-X (PCASP, Particle Measurement Systems) and Cloud Droplet Probe (CDP, Droplet Measurement Technologies Inc.) (Rosenberg et al., 2012; Sanchez-Marroquin et al., 2019). These instruments counted aerosol particles in the nominal diameter ranges of 0.12–2.5 μm and 5.6–67 μm respectively, these bin sizes were determined by a calibration procedure described in Price et al. (2018) and Rosenberg et al. (2012). Using this size-distribution

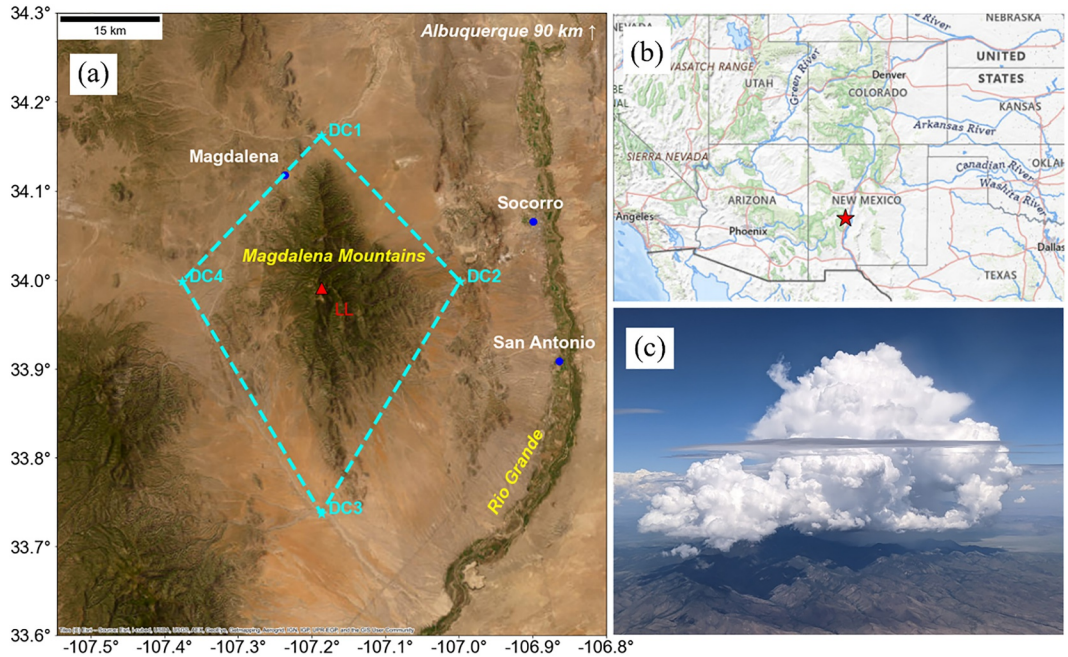

Figure 1. Study site context. (a) Typical aerosol sampling circuit around waypoints DC1–DC4 around Magdalena Mountain, its summit and location of Langmuir Laboratory (LL) denoted by red triangle (basemap source: Esri World Imagery). (b) Fieldwork location map (basemap source: OpenStreetMap). (c) Photograph taken from aircraft of convective cloud above the Magdalena Mountains during flight C308 (31st July 2022).

data, values were calculated for total aerosol number concentration and surface area and mass concentration assuming spherical geometry and density of 2.6 g cm^{-3}. They were also corrected to standard temperature and pressure (273.15 K and 1,013.25 hPa) and screened to exclude data where the ambient relative humidity (RH) exceeded 80%.

During the airborne campaign, aerosols were collected on filters for offline analysis of INP concentration spectra (INP concentrations as a function of temperature that the particles were exposed to while immersed in water droplets) and compositional assessment. Details of each filter run are shown in Table A1. Sampling was conducted via a pair of identical inlets located outside the skin on the port side of the aircraft and aligned with local airflow to allow sampling inside the cabin on two filters simultaneously. The inlet system includes a bypass, which is left open for all sampling described here, as this enhances flow at the inlet nozzles, so to minimize sub-isokinetic enhancement of supermicron particles (Sanchez-Marroquin et al., 2019). Typically, we used polycarbonate track-etched membranes with a 0.4 μm pore diameter (Whatman-Nucleopore 10417112) behind one inlet and Polytetrafluoroethylene (PTFE, referred to as PTFE from herein) membranes with a 1.2 μm effective pore diameter (Sartorius type 11806) behind the other. The polycarbonate filters were used for Scanning Electron Microscopy size resolved composition analysis (Sanchez-Marroquin et al., 2019). Both the polycarbonate and PTFE filters were used without pre-cleaning for INP analysis; the respective techniques for analyzing each type of filter are described below. Filters were loaded into the aircraft filter holders within a laminar flow hood. Filter holders, including the metal mesh supports, were cleaned after each flight by immersion in a sonic bath in ultra pure water, then rinsed with water and isopropanol, followed by being blown dry with an anti-static gun (Yuchengtech) supplied with oil free compressed air that had been passed through a HEPA filter. The laminar flow hood was lined with aluminium foil to reduce the build of static charge. Sampling durations typically ranged from 10 to 20 min with the volume of air sampled varied depending on sampling duration, altitude, and filter type, ranging from 114–987 L for PTFE filters and 78–341 L for polycarbonate filters (see Table A1). Flow volumes were measured on each inlet using an in-line mass flowmeter and datalogger (volumes are reported at standard temperature and pressure). Comprehensive characterization of this sampling system is provided by Sanchez-Marroquin et al. (2019), with previous applications in INP sampling detailed in Price et al. (2018) and Sanchez-Marroquin et al. (2021).

21698996, 2026, 3, Downloaded from https://agupubs.onlinelibrary.wiley.com/doi/10.1029/2024JD043236 by University Of Leeds The Brotherton Library, Wiley Online Library on [11/02/2026]. See the Terms and Conditions (https://onlinelibrary.wiley.com/terms-and-conditions) on Wiley Online Library for rules of use; OA articles are governed by the applicable Creative Commons License

21698996, 2026, 3, Downloaded from https://agupubs.onlinelibrary.wiley.com/doi/10.1029/2024JD043236 by University Of Leeds The Brotherton Library, Wiley Online Library on [11/02/2026]. See the Terms and Conditions (https://onlinelibrary.wiley.com/terms-and-conditions) on Wiley Online Library for rules of use; OA articles are governed by the applicable Creative Commons License

Nearly all aerosol run heights listed in Table A1 yielded both polycarbonate and PTFE filters, except on July 19th and 20th, where 2 PTFE filters were collected at each height, excluding polycarbonate filters to ensure equivalent sampling from both filter channels. Blank filters, comprising one polycarbonate and one PTFE filter each, were included in each flight to establish the limit of detection or INP concentrations. These blank filters were prepared and loaded into the sampling system and exposed to ambient air for approximately 1 s.

2.2. INP Concentration Spectra Analysis

INP concentration spectra (INP concentration as a function of temperature) for each filter sampling run were determined using droplet freezing assays. To expedite analysis, a temporary laboratory for clean handling of filters and droplet freezing assays was established in a dedicated hotel room in Albuquerque, enabling analysis of PTFE filters within 24–48 hr of collection. This minimizes any changes in the sample on storage and transport that have been reported previously (Beall et al., 2020), and also allows us to check handling blanks on campaign and adjust the experimental protocol where necessary. Polycarbonate filters were stored in airtight filter cassettes at −20°C and transported to the University of Leeds (at room temperature for a duration of 3–5 days before returning to −20°C) for droplet freezing assays and SEM analysis. To reduce the possibility of contamination in the hotel room lab, we used a HEPA air purifier system. We also installed an anti-static fan to reduce the build-up of static charge that can impact the handling of filters.

We used the µl-NIPI (Nucleation by Immersed Particles Instrument) for the INP filter analysis (Price et al., 2018; Whale et al., 2015). µl-NIPI consists of a Stirling engine cooled cold plate and a perspex chamber that sits atop the cold plate. Compressed air (which had been passed through a HEPA filter and a Dryerite column in the hotel room lab) or dry nitrogen gas from a cylinder (in Leeds), was passed through the perspex chamber to prevent contamination and eliminate frost formation. A digital camera was used to record images and the cold stage temperature was recorded on a computer. The way in which the cold stage is used to analyze INP on the two filter types differs as follows.

The hydrophobic nature of PTFE filters facilitated the "drop-on" droplet freezing assay technique (Figure 3a), where typically 80–100 2 µL droplets of ultrapure water were directly placed on the exposed filter positioned on a cooling stage using an electronic pipettor (Price et al., 2018; Raif et al., 2024; Schnell, 1982). A 10 µL capacity pipette tip was used to dispense 5 × 2 µL droplets, which was refilled several times for each filter. One pipette tip was used per filter and disposed of after use.

Polycarbonate filters were analyzed for INP using the "wash-off" method (Figure 3b), which differs from the "drop-on" approach by using immersion in ultrapure water to create a suspension. We subsequently pipetted typically 40–60 1 µL droplets of this suspension onto a clean substrate mounted on a cold stage (O'Sullivan et al., 2018; Whale et al., 2015). The droplet freezing assay records the fraction of droplets frozen as a function of temperature, used to calculate INP per liter of air (N_{INP}) using equations adapted based on the filter type. For PTFE filters,

$$N_{INP} = -\ln\left(1 - F(T)\right)\frac{A_{fil}}{V_s \alpha}, \quad (1)$$

where F is the fraction of droplets frozen at temperature T, A_{fil} is the area of exposed filter (11 ± 2 cm^2), α is the area "footprint" of the droplet contacting the exposed filter (0.136 cm^2 for 2 µL droplets), and V_s is the volume of air sampled, converted to standard temperature and pressure. For polycarbonate filters:

$$N_{INP} = -\ln\left(1 - F(T)\right)\left(\frac{V_w}{V_a x V_s}\right) \quad (2)$$

where V_w is the volume of water the aerosol is washed into, V_a is the volume of the droplets, and x is the fraction of filter used in the analysis. As the "drop-on" droplet freezing assay technique with PTFE filters does not involve dilution of the aerosol particles when washed off and suspended in water, it has higher sensitivity sampling of INPs (~0.01–10 L^{-1}) compared to the wash-off method (~1–100 L^{-1}) from the relatively short sampling times available. This extends the range of detectable INP concentrations to higher temperature (>−10°C in this campaign), including the temperature range of −3 to −7°C where the Hallett-Mossop SIP process is thought to be

21698996, 2026, 3, Downloaded from https://agupubs.onlinelibrary.wiley.com/doi/10.1029/2024JD043236 by University Of Leeds The Brotherton Library, Wiley Online Library on [11/02/2026]. See the Terms and Conditions (https://onlinelibrary.wiley.com/terms-and-conditions) on Wiley Online Library for rules of use; OA articles are governed by the applicable Creative Commons License

most efficient (Hallett & Mossop, 1974). Background subtraction of INP data was performed using handling blank data (Figure 3), producing final INP data binned in 0.5°C intervals using the approach described in Appendix A of Sanchez-Marroquin et al. (2023). Briefly, we converted cumulative fraction frozen data for samples and the handling blanks into the differential INP spectrum, $k(T)$, representing INPs activated per temperature interval (Vali, 1971, 2019). Where the lower error of a $k(T)$ data point of a temperature interval for a sample was not higher than the upper error of $k(T)$ points of the handling blanks (three times the standard deviation of all blank $k(T)$ values), we considered the point as consistent with background, and thus an upper limit. We then reconstructed the cumulative INP spectrum using these corrected k values. For data above the detection limit, background values were subtracted and then reconstructed the cumulative $K(T)$ spectrum, and then N_{INP} spectrum using these corrected k values.

2.3. Aerosol Composition by Scanning Election Microscopy With Energy Dispersive Spectroscopy (SEM-EDS)

Automated analysis of individual aerosol particles sampled on polycarbonate filters used SEM-EDS (Sanchez-Marroquin et al., 2019) to determine the size-resolved elemental composition of particles with diameters larger than 0.3 μm. The purpose of this technique is to identify and quantify different aerosol populations based on their composition and size distribution. Sections of filters from selected sample runs were mounted on 25 mm diameter stubs with adhesive surfaces and sputter-coated with 30 nm of iridium or platinum before SEM analysis (Tescan VEGA3 XM fitted with an X-max 150 SDD energy-dispersive X-ray spectroscopy) at the University of Leeds. The microscope, controlled by feature recognition and classification software (Aztec 3.3, Oxford Instruments), enabled the individual scanning and automatic classification of thousands of particles per filter into size-binned compositional classes such as mineral dust, carbonaceous, and sulphate-rich particles. No elemental classification for biological particles was used, partly due to the coincidence of the EDS peaks for the bio-marker element phosphorus with those of iridium or platinum used for coating. Therefore, such particles were classified as carbonaceous. Some primary biological particles (PBABs), like pollen, spores, or intact bacteria, could be qualitatively identified by eye based on their relatively larger sizes and their morphology. These, and other large but rare particle types, were mostly noted during manual surveying of the filter, rather than during the automated analysis procedure, which typically covers a very small swathe of the filter.

2.4. Ground-Based Meteorological Observations

Ground-based weather observations were made to record the general meteorological conditions at the study area over the full duration of the DCMEX flight campaign (16th July–8th August 2022). A Vaisala WTX536 station was installed close to the Langmuir Laboratory at Kiva-2 on South Baldy peak (33.991 N, 107.187 W) which is the highest point of the Magdalena Mountains at 3,290 m ASL, and recorded temperature, pressure, relative humidity, windspeed and wind direction.

2.5. Cloud Ice-Particle Number Concentration Measurements

In addition to the filter sampling, the DCMEX flights included cloud penetration runs where microphysical measurements were made including ice particle detection and counting (Finney et al., 2024). This provided an opportunity to measure ice-particle number concentrations (N_{ice}) and directly relate them to the measured out-of-cloud INP concentrations. Relating primary ice concentrations in rising cloud turrets to INP concentrations is a crucial step in quantifying secondary ice-production processes. Capturing the transition of no-ice detection to first detection of ice crystals in tops (within ∼100 ft of cloud top) of rising cloud turrets provides some confidence that the ice crystals are primary, that is, directly formed from the INP present rather than influenced by sedimentation or entrainment from other regions of the cloud. A limitation of this method is that the in-cloud temperature measurements are uncertain due to wetting of the aircraft temperature sensor (Lloyd et al., 2020). Other factors affecting the estimates are: (a) the fact that updrafts may be positively buoyant with a temperature 1 or 2°C greater than the environmental values; (b) evaporation will result in downdrafts being colder than the environment; and (c) the altitudes of the tops of turrets were estimated using calculations from the forward-facing camera images with reference to the altitude of the aircraft. The N_{ice} of each cloud pass was measured using a High Volume Precipitation Spectrometer-3 (SPEC Inc, Boulder, USA, hereon HVPS), a high-speed stereographic photodiode imaging probe mounted underneath the aircraft wing which images and classifies hydrometeors in the range 0.15–19 mm with a resolution of 150 μm, based on their irregularity of shape (Crosier et al., 2011; Finney et al., 2024;

21698996, 2026, 3, Downloaded from https://agupubs.onlinelibrary.wiley.com/doi/10.1029/2024JD043236 by University Of Leeds The Brotherton Library, Wiley Online Library on [11/02/2026]. See the Terms and Conditions (https://onlinelibrary.wiley.com/terms-and-conditions) on Wiley Online Library for rules of use; OA articles are governed by the applicable Creative Commons License

Lawson et al., 2006; Lloyd et al., 2020). Of the array of cloud physics instruments used on DCMEX (Finney et al., 2024), the HVPS is the most suited to detection of first cloud ice particles due to its larger sampling volume, 310 L at an airspeed of 100 m s^{-1}. After conversion of the sample volumes to standard temperature and pressure, the detection limit of ice crystals larger than 150 μm diameter on this campaign was around 0.005–0.008 L^{-1}, which is comparable to that of our PTFE filters method for N_{INP} quantification, allowing for direct comparison.

3. Results and Discussion

3.1. Aerosol Structure and Meteorological Conditions

The vertical profiles of the atmosphere in the vicinity of the Magdalena Mountains in terms of accumulation to coarse mode (0.2–67 μm diameter) aerosol load, were constructed from whole-flight rolling 30-s averages of PCASP and CDP concentrations (Figures 2a and 2b and for individual flights in Figure S1 of the Supporting Information S1). Ground-based meterological observations from Langmuir Laboratory, are also shown in Figure 2c and Table S1 of the Supporting Information S1. The vertical aerosol profiles illustrate a consistent transition from a high aerosol concentration (~500–800 cm^{-3}) to a much lower concentration (<100 cm^{-3}) between 4 and 6 km ASL (all heights expressed hereon are in ASL, unless stated otherwise). For simplicity, we refer hereon to the region below and above the transition as the high- and low-aerosol layers, respectively.

The time series of vertical aerosol profiles shown in Figure 2b illustrates that the depth of the high-aerosol layer varied over the campaign, reaching two maxima around 20th July and 4th August with the lowest depth occurring in the middle of the campaign. Overall, this high aerosol layer was well-mixed, although notably elevated coarse mode aerosol concentrations were observed between 3rd–6th August (C312–314, Figure S1 in Supporting Information S1), but otherwise the vertical profiles of aerosol mass concentration and number concentrations, indicating profiles of fine and coarse aerosol respectively (Figure S1 in Supporting Information S1) were constant within the high aerosol layer. Super-coarse and giant mode (above diameters of 10 and 62.5 μm, respectively (Adebiyi et al., 2023)) particles were typically observed only during the low-level terrain following runs.

We now compare the aerosol layer properties with trends in the meteorological conditions recorded at Langmuir Laboratory during the campaign, shown in Figure S7 of the Supporting Information S1. Early flights (C297–C300, 16th–22nd July) saw an initially hot, low humidity (14–22°C and 30%–50% RH) spell, replaced by cooler, more humid (10–16°C and 60%–80% RH) conditions (C300–C310, 22nd July–1st August), with moderately warmer and still humid (12–20°C and 50%–70% RH) conditions prevailing in the last third of the campaign (C309–C315, 1st–8th August). Most rainfall was concentrated during 23rd July–1st August when thunderstorms (as per lightning flashes detected within the sampling circuit by satellite (Finney et al., 2024)) were most frequent. ECMWF ERA5 reanalysis detailed in Finney et al. (2024) revealed that the synoptic situation can be summarized by the early hot and dry spell being associated with north-westerly anti-cyclonic winds from Arizona, transitioning into a moist, southeasterly flow originating from Texas and the Gulf of Mexico beyond. A weaker northerly flow briefly returned and was replaced again by moist, southerly flow during the latter third of the campaign. From Figure 2b it is apparent that the fluctuation of the aerosol layer depth coincides with average daily temperatures, responding to these changes in airmasses. This, and the presence of coarse aerosol up to 6 km, indicates that there is a residual boundary layer with well-mixed accumulation- and coarse-mode aerosol resulting from a combination of dry convection and wet convection with detraining aerosol layers over the course of days prior to the air arriving at the Magdalena mountains. Overall, this characterization enabled sampling of INP with contrasting altitudes, meteorological conditions and aerosol loads, in situ with convective cloud formation.

3.2. Ice-Nucleating Particle Measurements

For every flight, at least one filter sampling run was made within the high aerosol layer, as shown in Figure 2b. From flight C303 onwards, once the depth of the aerosol layer had been established, filter runs above the transition in the low-aerosol layer were also made. Fraction frozen plots with PTFE results, shown in Figures 3a and 3b, were between −5 and −20°C, well clear of handling blanks. Polycarbonate filters exhibited freezing between −20 and −28°C, with some as warm as −15°C. Their freezing spectra (Figures 3a and 3b) were closer to their respective handling blanks compared to the PTFE filters' spectra but were still significantly warmer. For both filter techniques, the droplet freezing temperatures broadly corresponded to the three sampling run levels (Figure 2), where warmer freezing temperatures were seen at lower levels, although there was little distinction between the mid-level and terrain-following PTFE data. The corresponding background subtracted INP

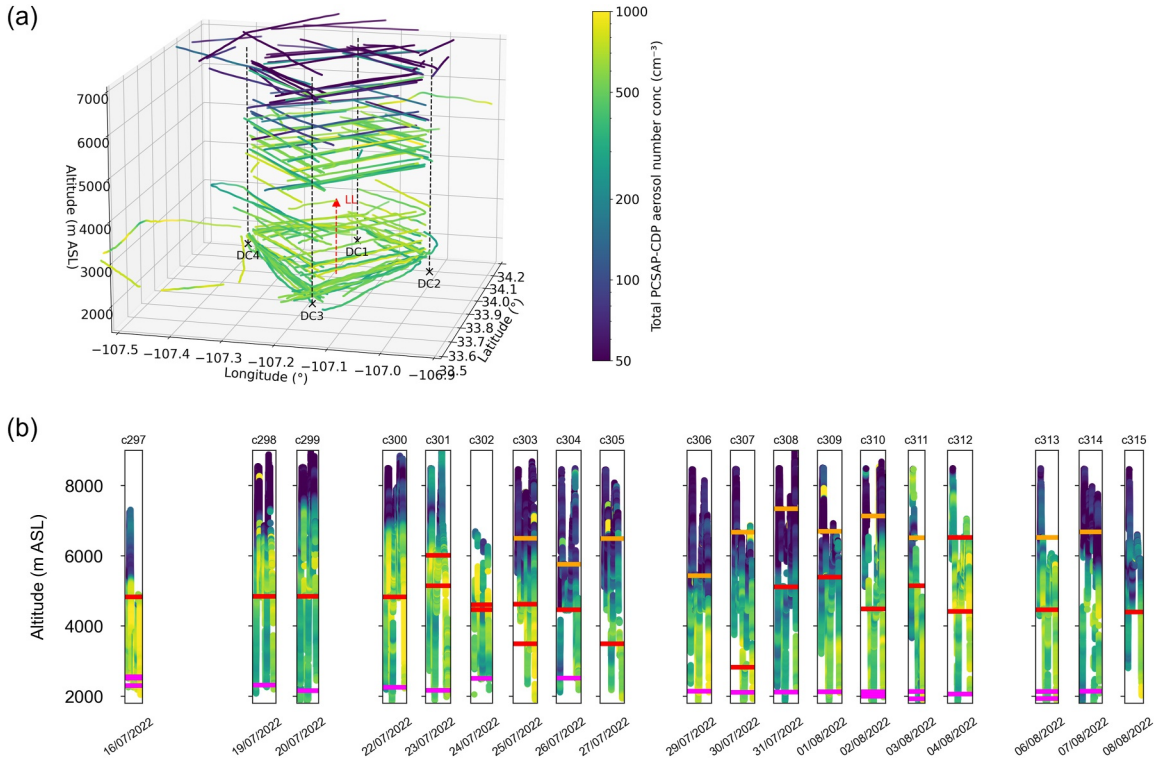

Figure 2. The vertical aerosol loadings and meteorology during DCMEX. (a) 3-D plan of sampling runs around the circuit DC1–DC4 showing vertical structure of PCASP+CDP derived aerosol and mass concentration. Location of Langmuir Lab (LL) is denoted by red triangle. (b) Time series of vertical particle number concentration, illustrating varying depth of High Aerosol layer. Colored lines indicate levels of INP sampling run: magenta for Terrain Following runs, red for Mid-Level runs and Orange for High Altitude runs.

concentration (N_{INP}) spectra for the polycarbonate and PTFE filters are shown in Figure 4a and in more detail in Figure S1 of the Supporting Information S1. Overall, there was good agreement when all runs are plotted, showing steeper slopes above −15°C and below −20°C, with a shallower section in between. However, in some cases the polycarbonate filters show lower INP concentrations above ∼−25°C and greater concentrations below ∼−25°C (see the individual comparisons in Figure S1 of the Supporting Information S1). In the latter case, this tended to occur for high altitude, low aerosol load sampling runs, so can be attributed to the data being close to the method detection limit and, as such, many of these data points have been flagged as upper limits (see e.g., C309R1, C310R1, C311R1, C312R1, and C314R1). In the former case, this is similar to results reported by Sanchez-Marroquin et al. (2021) for samples collected over southeast England, mainly affecting the warmest data points (see e.g., C297R1-4, C303R3, C309R3). The reasons for this may be due to changes occurring in transit where cold storage temperatures could not be maintained (Beall et al., 2020), but are consistent with technique-to-technique variability reported in the literature (Hiranuma et al., 2019; Wilbourn et al., 2024). To further investigate, we are conducting a set of controlled laboratory tests in our laboratory in Leeds.

Based on our INP measurements, we have developed a temperature-dependent N_{INP} parameterization to represent N_{INP} in conditions immediately preceding deep convective cloud development in a mid-latitude terrestrial setting, shown in Figures 4a–4c. The derivation of this parameterization is outlined fully in Appendix B. We compare our N_{INP} spectra with the Petters and Wright (2015) compilation of INP concentrations derived from precipitation samples from around the world, in Figure 4a. N_{INP} in DCMEX were largely consistent with the highest reported in the Petters and Wright compilation, and sometimes exceeded them, albeit with a similar shaped curve. When compared to the range of primary N_{ice} compiled by Cooper (1986), which also extends to slightly higher concentrations than the Petters and Wright range, our N_{INP} results show stronger agreement. The compilation of Cooper includes data from clouds in USA (Wyoming, Montana), Spain, Israel, South Africa and Australia, hence mostly representative of continental clouds in environments that are likely to have aerosol loadings that are comparable to those found in New Mexico.

21698996, 2026, 3, Downloaded from https://agupubs.onlinelibrary.wiley.com/doi/10.1029/2024JD043236 by University Of Leeds The Brotherton Library, Wiley Online Library on [11/02/2026]. See the Terms and Conditions (https://onlinelibrary.wiley.com/terms-and-conditions) on Wiley Online Library for rules of use; OA articles are governed by the applicable Creative Commons License

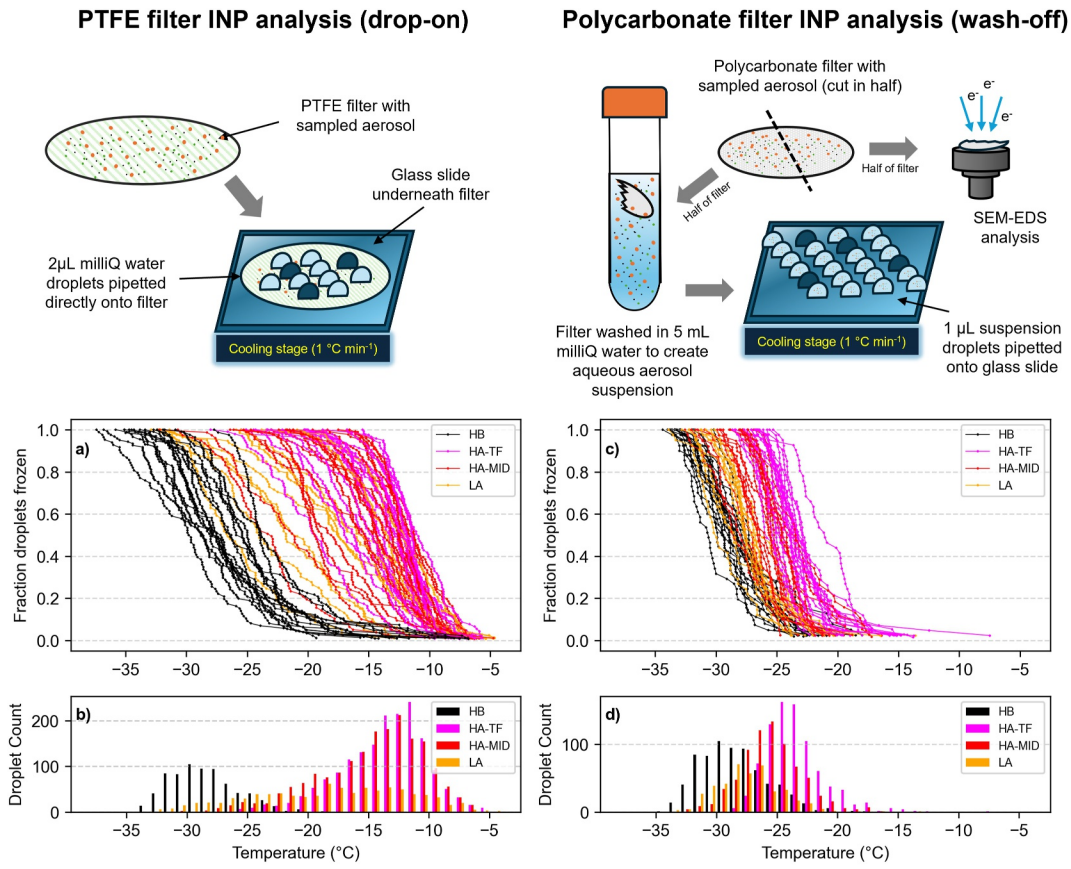

Figure 3. INP analysis method illustrations along with raw droplet freezing assay results including cumulative fraction frozen plots and histograms for PTFE (a, b) and polycarbonate (c, d) filters. Droplet data has been color coded to show comparison with handling blank (HB) and individual sampling levels shown in Figure 2 and Table A1: Terrain-following within the high aerosol (HA-TF) layer; mid-level runs within the high aerosol layer (HA-MID) and high altitude runs in the low aerosol layer (LA).

In Figure 4b, our measurements are compared with previous aircraft based INP sampling studies that used an identical methodology (the BAe-146 filter system and droplet-on-filter PTFE method), to compare our data with past measurements from environments with contrasting air-masses. These include within dust-laden Saharan Air Layer over the Atlantic (Price et al., 2018), biogenic particle laden air above the British Isles (Sanchez-Marroquin et al., 2021), late winter Arctic air containing Arctic haze around Svalbard (Raif et al., 2024) and late winter more pristine air in northern Alaska (Sanchez-Marroquin et al., 2023). It is apparent that these N_{INP} spectra have distinct characteristics at warmer and colder temperatures, consistent with dust load and proximity to sources of biologically derived INP. A striking comparison is with the Saharan Air Layer, where our N_{INP} is significantly lower at colder (<−20°C) temperatures but becomes higher at warm (>−15°C) temperatures, consistent composing of less mineral dust-laden, more biologically derived INP sources, such as, for example, terrestrial vegetation and organic rich, fertile soils. The two campaigns (Raif et al., 2024; Sanchez-Marroquin et al., 2023), from Arctic regions' data show lower N_{INP} than for DCMEX as expected, presumably related to the much lower ambient aerosol concentrations in those environments. Notably, the N_{INP} at warmer temperatures (above −10°C) shown by Raif24 and DCMEX, are comparable despite their contrasting sampling locations, in marine and terrestrial environments respectively.

To further contextualize our N_{INP} data, Figure 4c shows our data against past ground-based measurements of INP taken at comparable locations (mid-latitude sites in the continental USA) using a range of techniques (filters and online methods). Three studies—Garcia et al. (2012), Hiranuma et al. (2021), and Suski et al. (2018), were done during agricultural dust emission activities, such as crop harvesting, at rural sites in Texas, Kansas/Wyoming and Colorado/Nebraska respectively. Our data agrees well with the lower ranges of *Hiranuma*, *Garcia* and with *Suski*,

21698996, 2026, 3, Downloaded from https://agupubs.onlinelibrary.wiley.com/doi/10.1029/2024JD043236 by University Of Leeds The Brotherton Library, Wiley Online Library on [11/02/2026]. See the Terms and Conditions (https://onlinelibrary.wiley.com/terms-and-conditions) on Wiley Online Library for rules of use; OA articles are governed by the applicable Creative Commons License

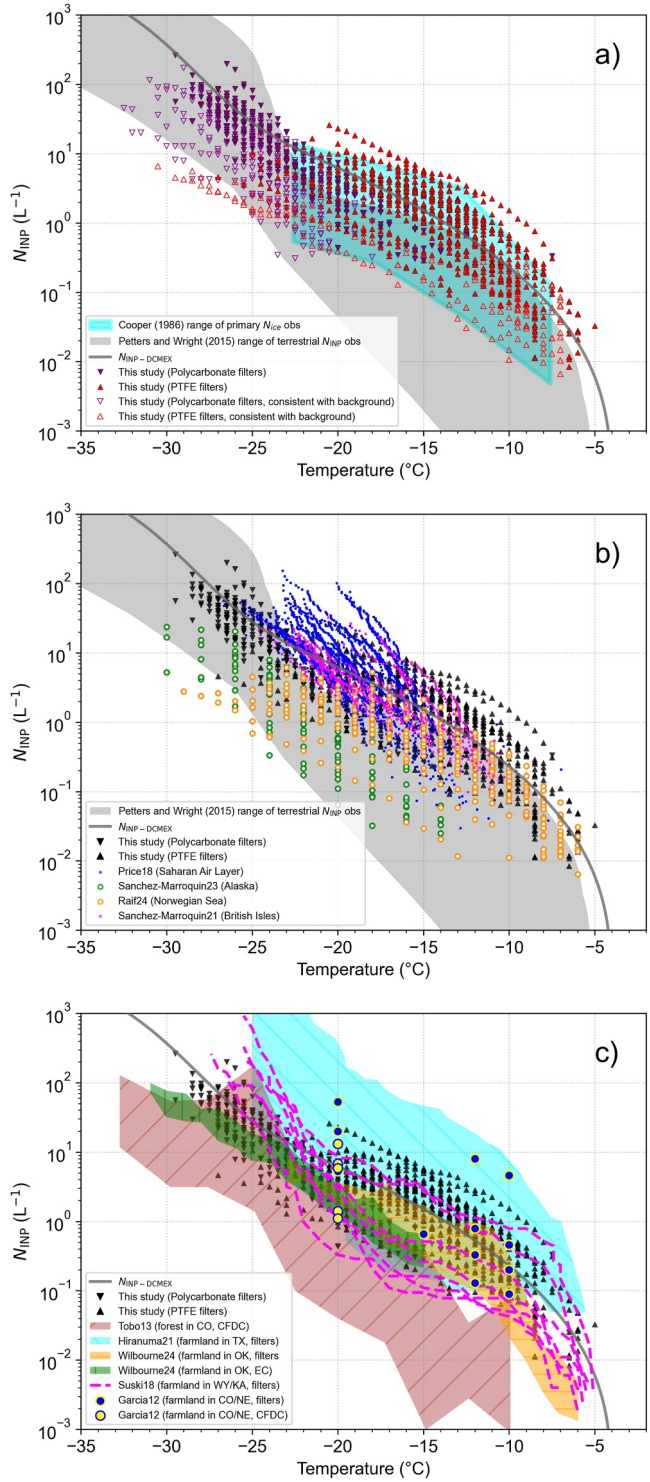

Figure 4. (a) All filter N_{INP} data (with upper-limit values indicated) and our parameterization $N_{INP\text{-}DCMEX}$ plotted against Petters and Wright (2015) range and Cooper (1986) range of primary cloud ice particle number concentrations from Figure 4.2 of that publication. (b) N_{INP} data (not including upper limits) from this study plotted against previous aircraft INP N_{INP} data taken in other locations using the same methodology. Note only PTFE filter data is available. (c) N_{INP} data (not included upper-limit data) from this study plotted with INP field data from various locations in mid-latitude USA. Key to INP sampling methods: Filters (offline, wash-off technique only); EC (online, Expansion Chamber); CFDC (online, Continuous Flow Diffusion Chamber).

21698996, 2026, 3, Downloaded from https://agupubs.onlinelibrary.wiley.com/doi/10.1029/2024JD043236 by University Of Leeds The Brotherton Library, Wiley Online Library on [11/02/2026]. See the Terms and Conditions (https://onlinelibrary.wiley.com/terms-and-conditions) on Wiley Online Library for rules of use; OA articles are governed by the applicable Creative Commons License

21698996, 2026, 3, Downloaded from https://agupubs.onlinelibrary.wiley.com/doi/10.1029/2024JD043236 by University Of Leeds The Brotherton Library, Wiley Online Library on [11/02/2026]. See the Terms and Conditions (https://onlinelibrary.wiley.com/terms-and-conditions) on Wiley Online Library for rules of use; OA articles are governed by the applicable Creative Commons License

Table 1
Summary of Vertical Distribution of N_{INP} and Aerosol Concentrations

	Mean number conc (cm^{-3})	Mean surface area conc ($\mu m^2\ cm^{-3}$)	Mean particle mass conc ($\mu g\ cm^{-3}$)	Mean particles >0.5 μm diameter (cm^{-3})	Median N_{INP} at −10°C (L^{-1})[a]	Median N_{INP} at −15°C (L^{-1})[a]	Median N_{INP} at −25°C (L^{-1})[b]
Terrain following, high-aerosol layer	524.2	52.5	25.5	0.96	0.13	1.63	24.1
Mid-level, high-aerosol layer	519.7	51.5	16.2	0.66	0.25	1.77	13.0
High-aerosol layer, all	522.0	52.0	21.0	0.81	0.15	1.70	16.7
Low-aerosol layer, all	66.4	5.9	2.2	0.12	0.32	1.46	4.80

[a]PTFE data set. [b]Polycarbonate data set.

tending to fall below it in the range colder than −20°C. Wilbourn et al. (2024), a longer-term data set from a rural site in Oklahoma not in direct influence of harvesting activity, shows comparatively lower N_{INP} so agrees very well with our polycarbonate data and with the lower sector of our PTFE data. In contrast, far lower N_{INP} were recorded at a remote forested site (Tobo et al., 2013) located in the Rocky Mountains in Colorado, with only the upper range of their values below around −15°C falling within agreement with our data. Overall, this suggests our N_{INP} data is consistent with environments influenced by dust emissions from fertile soils, which likely contribute to the aerosol load above the Magdalena Mountains.

The vertical structure of N_{INP} and aerosol populations is summarized in Table 1 and plotted on an individual flight basis in Figure S1 of the Supporting Information S1. To further analyze any relationships between N_{INP} and environmental factors we performed a Spearman's rank correlation analysis of N_{INP} at −10°C, −15°C (PTFE data set) and −25°C (polycarbonate data set) with the mean aerosol concentrations during each respective run, and with meteorological conditions recorded at the summit of Magdalena Mountains at Langmuir Laboratory during the flights. We included N_{INP} datapoints that were considered upper limits in the analysis as excluding these would bias the data set against sample runs taken under lower aerosol loads. In summary, N_{INP} responded to changes in the depth of the aerosol layer as depicted in Figure 2, particularly at colder (below −15°C) temperatures. However, within the aerosol layer, we found little apparent relationship within the PTFE data set between N_{INP} and changes in meteorological conditions over the course of the campaign. No correlations were found with N_{INP} at −10 or −15°C, except for altitude (+0.38) with N_{INP} at −10°C. In contrast, the polycarbonate N_{INP} data at −25°C showed a dependence on aerosol load, with significant positive (+) or negative (−) correlations of N_{INP} at −25°C with aerosol number, surface area and mass concentration (+0.53, +0.56 and +0.55 respectively). A cluster of correlations with meteorological variables—temperature (+0.51), dewpoint (−0.36), and relative humidity (−0.52)—suggest the hot and dry airmasses were associated with increased low-temperature INP, consistent with mineral dust aerosol. To further illustrate this, in Figure 5a, we colored the individual N_{INP} spectra according to the PCASP + CDP aerosol number concentration (i.e., >100 nm) while in Figure 5b we color code according to altitude. Trends of N_{INP} with aerosol concentration and altitude appear to be different above and below about −22°C, suggesting a change in the nature of the INP population. Finally, notable is the persistent presence of INP active warmer than −10°C on PTFE filters collected at elevated altitude, in the low-aerosol layer runs C303R1, C304R1, C305R1, C306R1, C307R1, and C308R1. However, we note that their incidence coincided with the depth of the aerosol layer reaching its shallowest point around 27th–29th July (Figure 2b), after which they were no longer detected.

Within the High Aerosol layer there is no clear altitude dependence of the N_{INP} spectra above around −22°C, with very similar shaped spectra varying only within about 1 order of magnitude. Also, there is little difference between terrain following runs close to the surface and runs at near the top of the high-aerosol layer, despite the terrain following runs having additional super-coarse INP (>10 μm). Much of the super-coarse aerosol larger than 20 μm in diameter may well be lost in the inlet system (Sanchez-Marroquin et al., 2019), but even if it were to make it through onto the filters, the analysis in Adebiyi et al. (2023) suggests it would play a minor role in

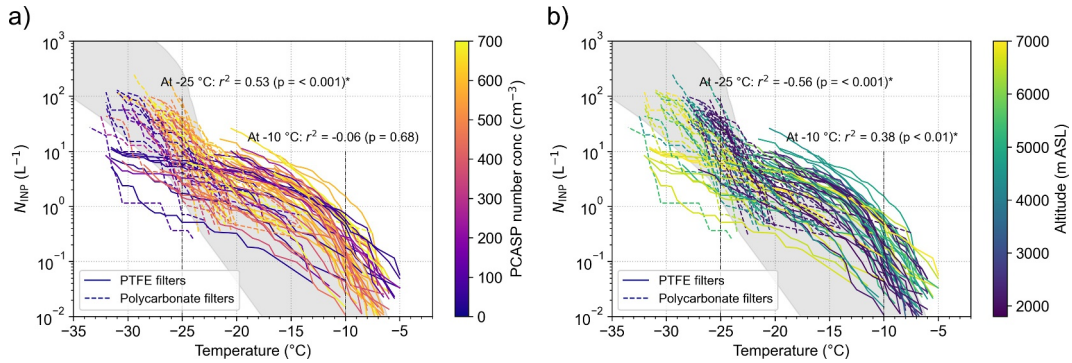

Figure 5. Vertical structure of N_{INP} concentrations (with upper limit data included) by (a) aerosol number concentration and (b) altitude. In both plots, the Spearman's rank correlation coefficients (r^2) between each variable and N_{INP} at −10°C and −25°C. Significance of correlation' p-number at 95% is denoted by *.

contributing to the N_{INP} because the number density is so low. The fact that the spectra showed little variability through the vertical profile in the high-aerosol layer indicates that the INP (and <10 μm aerosol) were well mixed throughout this layer.

Above 6 km ASL (i.e., in the low aerosol layer), the INP spectra were often a lot flatter and include some of the highest N_{INP} at > −10°C reported in DCMEX, despite having lower total aerosol concentrations. Coarse mode aerosol was typically about an order of magnitude less concentrated but still consistently present in the low-aerosol layer (Table 1 and Figure S1 in Supporting Information S1), indicating that this aerosol had been transported here within days of the measurement, according to the expected residence time of these size particles. Below approximately −23°C, the N_{INP} scale with aerosol number concentration and altitude with the highest N_{INP} being found where the aerosol concentrations were the greatest. This indicates that there are two populations of INP with different dependencies on the aerosol number. As discussed further below, the INP active below −23°C may be related to the abundant accumulation mode mineral dust particles, hence it scales with aerosol load. In contrast, above −23°C there is some other INP type that make up a small proportion of the overall aerosol population and has a distinct source to the bulk of the aerosol particles; hence it does not correlate with overall aerosol concentration.

3.3. Size-Resolved Composition and Ice-Nucleating Ability of Aerosol

We conducted SEM analysis on five filter samples, all collected within the high-aerosol layer. Three samples were from low altitude terrain-following runs (C301R2, C306R2, C307R2), and two were from altitudes of around 4.5 km (C302R1 and C312R2). The SEM data, summarized in Figures 6 and 7; Figure S6 in Supporting Information S1 showed very good agreement with the aircraft PCASP-CDP measured aerosol particle size distributions, except at the finest (<0.4 μm) end, where SEM sometimes underpredicted particle counts. The undercounting relative to the optical probes has been observed before (Sanchez-Marroquin et al., 2019), and may be due to the loss or shrinking of non-refractory particles in the SEM vacuum.

There was only minor variation in terms of super-micron particle composition between the samples, where they were dominated by mineral dust (Si-rich, Si-Al-rich, and Ca-rich particles; Figure 6a). Further analysis of this fraction indicates compositionally distinct populations of mineral dust, with an Si dominated (lacking Al) population tending to exist at submicron sizes and Si-Al rich particles existing at larger sizes, indicative of aluminosilicates. This distribution is comparable to that seen using this technique to the Saharan Air Layer filters in Price et al. (2018), yet with a higher proportion of carbonaceous particles, but lower than that seen over the British Isles in Sanchez-Marroquin et al. (2021). Sea salt particles were rare, consistent with being far from marine sources.

In addition to automatically detected particles, rare large (>20 μm) particles were observed in all samples, although in too small numbers to quantify robustly (examples in Figure 6a; Figures S2–S5 in Supporting Information S1). These included aggregates of aluminosilicate grains, up to 50 μm in diameter, observed on the low-level filter runs as well as on C312R2, a sample taken on one of the dustier days. Primary Biological Aerosol

21698996, 2026, 3, Downloaded from https://agupubs.onlinelibrary.wiley.com/doi/10.1029/2024JD043236 by University Of Leeds The Brotherton Library, Wiley Online Library on [11/02/2026]. See the Terms and Conditions (https://onlinelibrary.wiley.com/terms-and-conditions) on Wiley Online Library for rules of use; OA articles are governed by the applicable Creative Commons License

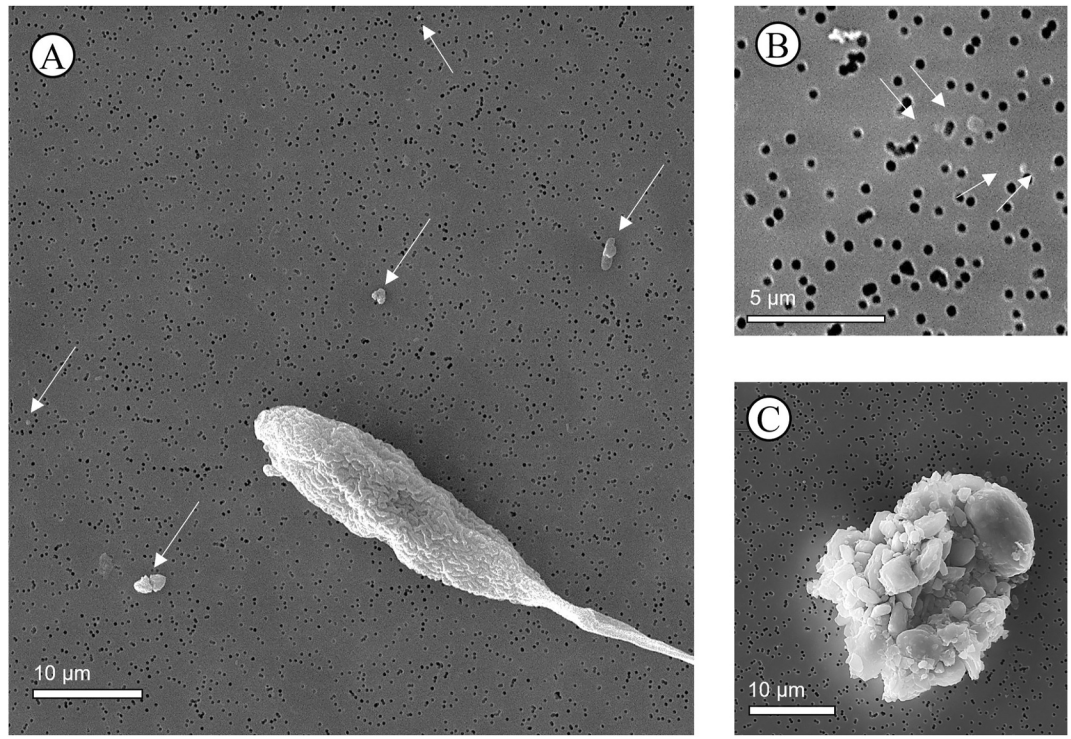

Figure 6. Summary of SEM analysis of particles on polycarbonate filters. Images taken from filter C306R2; black spots are the 0.4 µm filter pores. (a) Example of primary bioaerosol particle and smaller coarse-mode mineral dust, denoted by arrows. (b) Submicron particles of sulphate and carbonaceous composition, denoted by arrows. (c) Super-coarse (>10 µm) silicate particle aggregate.

Particles (PBAP), such as pollen grains and possible spores were observed but were rarer still, only observed on low-level run filters. A similar trend was seen from analysis of filters collected above the British Isles by Sanchez-Marroquin et al. (2021), where PBAPs were observed but only on sampling runs lower than 0.5 km, with concentrations seen of 5–25 particles per mm^2 of filter. However, here we estimate that our samples contained at least an order of magnitude fewer PBAPs than that study, with an upper limit estimated from the sample with most particles (C306R2), with around 1 per mm^2 by manually identified particles. Whilst these images demonstrate there is a source of biological aerosol that may function as INPs in convecting airmasses, there is no obvious enhancement in N_{INP} observed in runs where possible PBAPs were present. Moreover, we also note that N_{INP} from DCMEX were greater than those from the British Isles (Figure 4b), despite a considerably lower abundance of PBAPs.

This SEM-EDS data is crucial for testing if the observed N_{INP} can be explained by its composition, which in the case of particles over 0.5 µm in diameter, is dominated by silicate mineral dust. We calculated the ice-nucleating ability of the aerosol in terms of the density of active sites per unit area as a function of temperature, n_s, using Equation 3:

$$n_s = \frac{N_{INP}}{s} \tag{3}$$

where s is the surface area of the aerosol acting as INP. To test the hypothesis that the mineral dust component controls the ice nucleating activity of the aerosol we sampled in DCMEX we derive n_s using the surface area of mineral dust. This means we can then compare the derived n_s values to parameterizations of the activity of pure mineral components and natural soil dusts. This analysis implicitly discounts any contributions of ice-nucleating activity from the sulphate, carbonaceous, and metallic fractions, which are thought to have much lower or no ice-nucleating activity (Kanji et al., 2017). The mineral dust surface area was derived by summing the proportions of Si-rich, Ca-rich, Al-Si rich, and Si-only particle classes in each particle bin and multiplying by the number

21698996, 2026, 3, Downloaded from https://agupubs.onlinelibrary.wiley.com/doi/10.1029/2024JD043236 by University Of Leeds The Brotherton Library, Wiley Online Library on [11/02/2026]. See the Terms and Conditions (https://onlinelibrary.wiley.com/terms-and-conditions) on Wiley Online Library for rules of use; OA articles are governed by the applicable Creative Commons License

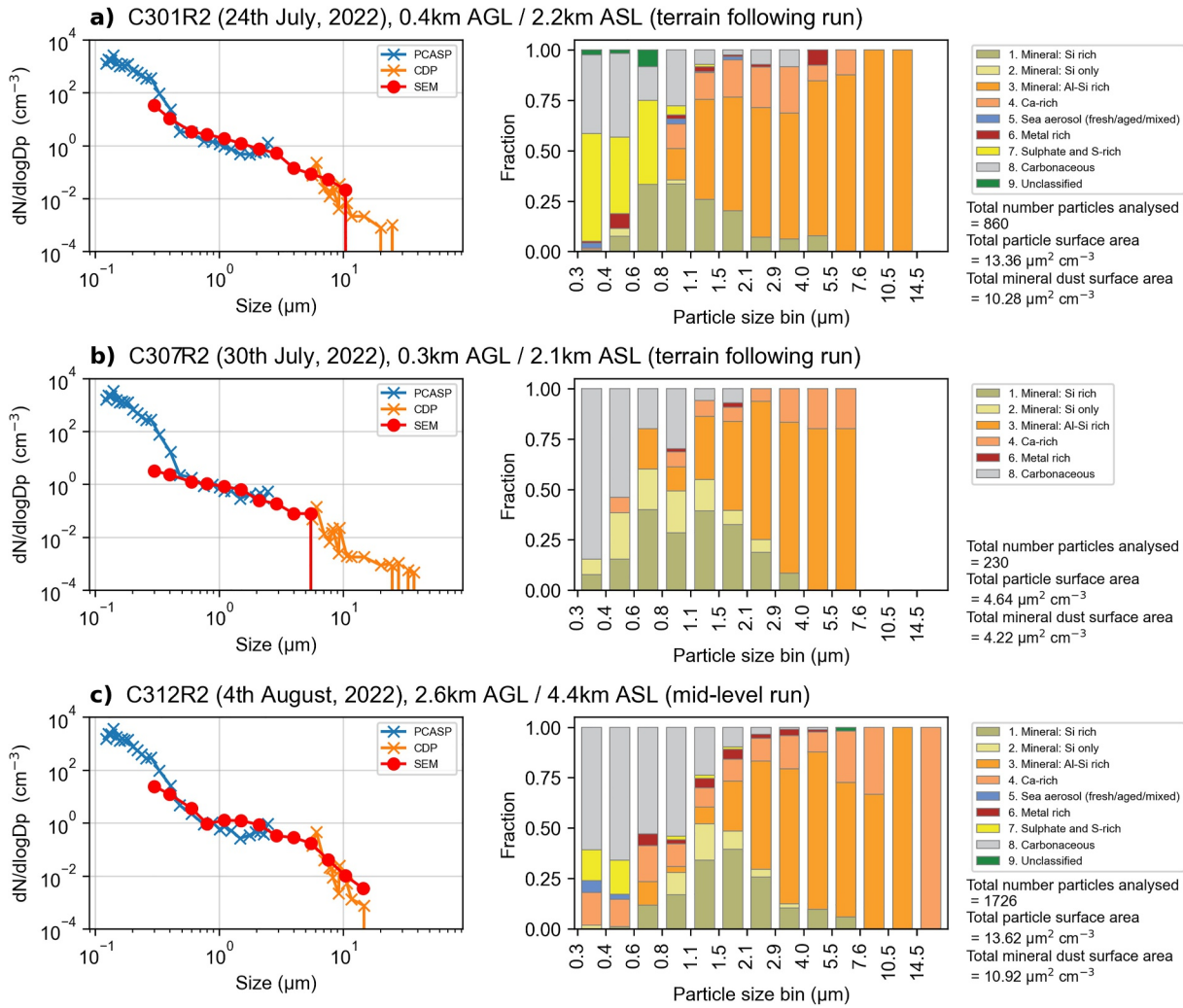

Figure 7. SEM automated particle analysis results for polycarbonate filters selected as examples of terrain-following runs (C301R2 and C307R2) and a mid-level run (C312R2): Left column: Particle number distribution compared to PCASP-CDP data; Right column: Box plots showing detailed proportional particle composition. For other examples, see Figure S6 in Supporting Information S1.

concentration. This typically ranged between about 5 and 10 μm^2 cm^{-3}, or roughly 10% of the total PCASP/CDP calculated aerosol surface area.

We plotted n_s derived from both PTFE and polycarbonate filter N_{INP} data for the samples that were analyzed with SEM-EDS, shown in Figure 8 alongside laboratory-derived n_s spectra for abiotic mineral dust with 5% K-feldspar (Harrison et al., 2019, 2022) and parameterizations for natural arid soil dust (from the ground and wind-blown dust) (Niemand et al., 2012) and fertile soils (O'Sullivan et al., 2018; Steinke et al., 2016; Tobo et al., 2014). We found that the n_s of the INP sampled in DCMEX was consistent with the various arid and fertile dust and the highest fertile (Steinke et al., 2016) parameterizations above −25°C. Below −25°C, these parameterizations converge and become indistinguishable, against which our n_s data is consistent. Fertile soils are characterized by an ice nucleating activity that rises several orders of magnitude greater than would be expected for abiotic mineral dusts from temperatures above about −25°C, attributed to the presence of biogenic proteinaceous ice-nucleating substances (O'Sullivan et al., 2014). Notably, PTFE and polycarbonate derived n_s data are largely consistent with this observation, supporting their agreement as comparable techniques in this study despite the discrepancies noted above. Overall, the n_s data presented here shows the INP sampled during DCMEX is consistent with fertile soils or arid soils with biogenic INP contributions. Heating tests can be used to indicate the presence of heat-labile proteinaceous INP by deactivating INP activity at warm (>15°C) temperatures (Daily et al., 2022). Unfortunately, the PTFE filters we used are incompatible with this test as the collected aerosol cannot be washed from them.

21698996, 2026, 3, Downloaded from https://agupubs.onlinelibrary.wiley.com/doi/10.1029/2024JD043236 by University Of Leeds The Brotherton Library, Wiley Online Library on [11/02/2026]. See the Terms and Conditions (https://onlinelibrary.wiley.com/terms-and-conditions) on Wiley Online Library for rules of use; OA articles are governed by the applicable Creative Commons License

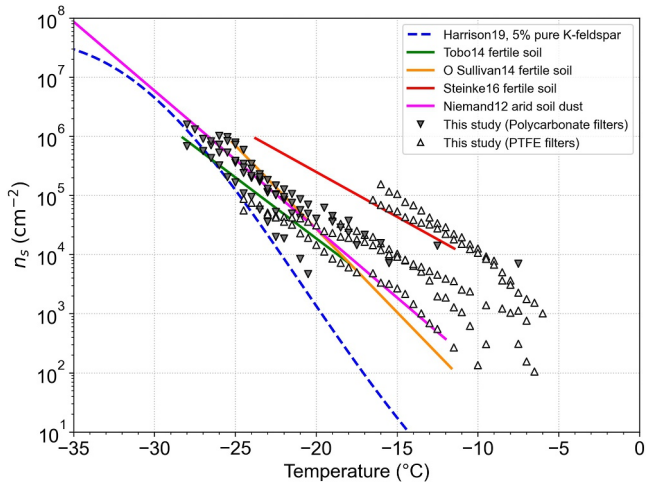

Figure 8. Active site density (n_s) of our INP samples normalized to mineral dust surface area, as quantified by SEM analysis. Literature n_s parameterizations for abiotic mineral dust, and natural arid and fertile soils are shown for comparison. Data is shown for all sampling runs where SEM analysis was performed on the polycarbonate filter: C301R2, C302R1, C306R2, C307R2, and C312R2.

Consequently, further characterization of high-temperature INP and their atmospheric distribution is a priority for future study.

3.4. Comparison of Ice-Nucleating Particle Observations With Ice Particle Number Concentrations in New Convective Cloud Turrets

In principle, the INP concentration defines primary ice production in clouds warmer than ∼−35°C. However, experimental evidence for this relationship is lacking from the literature because suitable clouds passes have not been made on the same flights as robust measurements of INP spectra (e.g., Lloyd et al., 2020; Yang et al., 2020; Zaremba et al., 2021). There were a number of flights in DCMEX where the aircraft repeatedly passed through growing congestus turrets at sequentially higher altitudes and lower temperatures, in which we initially saw no ice on the first passes but began to detect ice on subsequent passes.

To compare N_{INP} with N_{ice} we contrast N_{ice} determined from the HVPS instrument during cloud passes to N_{INP} spectra that were recorded earlier in the flight in air representative of air that was ingested into the convective cloud. To determine N_{ice} we used data from the HVPS instrument because it has a large sample volume (and therefore a lower detection limit relative to other instruments such as the 2D-S), but its resolution limits the detection of ice to particles larger than 150 μm. Consideration of ice crystal growth time scales is important for the interpretation of the cloud pass N_{ice} values, as freshly nucleated ice crystals need time to grow to sizes detectable by the HVPS during the cloud pass. Literature data suggest that in the basal growth regime at ∼−6°C it takes around 150 s to reach 150 μm, whereas at the peak of the prismatic face growth regime at ∼−16°C it takes around 50 s. In contrast, there is a minimum in growth rate between ∼−8 and −12°C and the time to grow to 150 μm is expected to exceed ∼10 min (Fuchs et al., 2025; Ryan et al., 1976). Hence, if out-of-cloud INP spectra defines primary ice production in the cloud, and no secondary ice processes have had time to occur, we would expect to see the HVPS derived N_{ice} equal to or below the N_{INP}. While secondary ice production processes cannot be completely ruled out, their typical indicators, such as the co-occurrence of supercooled raindrops or rimed graupel (Field et al., 2017), were not observed in the cloud passes reported here.

Two flights lent themselves to the cloud-pass analysis, C301 and C304, in which we had INP spectra and successive cloud passes over a range of altitudes. Cloud penetration passes were made as close to the tops of turrets as possible (within 200 m), ascending from approximately 5 km up to 9 km ASL, where the out-of-cloud temperatures ranged between approximately 0 and −22°C respectively. Note that in-cloud temperature measurements from FAAM are known to be affected by wetting of the sensor (Lloyd et al., 2020), hence we report nearby out of cloud temperatures at the same altitude. The in-cloud temperature is typically thought to be within ∼2°C of the out-of-cloud temperature (Lloyd et al., 2020). A photograph of a turret immediately before one of these clouds

21698996, 2026, 3, Downloaded from https://agupubs.onlinelibrary.wiley.com/doi/10.1029/2024JD043236 by University Of Leeds The Brotherton Library, Wiley Online Library on [11/02/2026]. See the Terms and Conditions (https://onlinelibrary.wiley.com/terms-and-conditions) on Wiley Online Library for rules of use; OA articles are governed by the applicable Creative Commons License

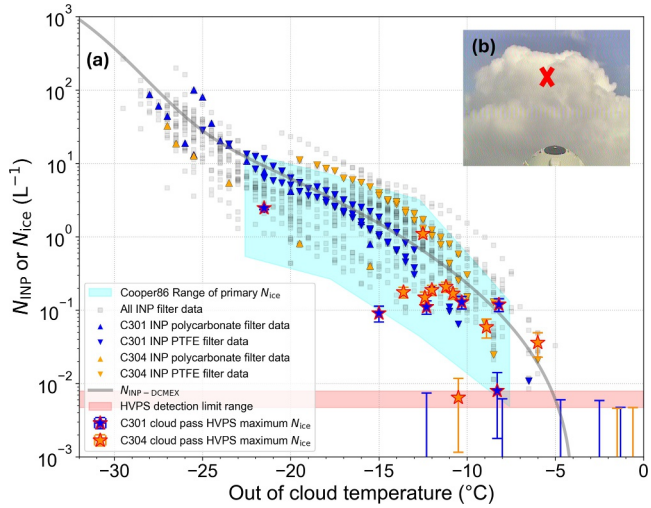

Figure 9. (a) Comparison of cloud N_{ice} measured using the HVPS during cloud penetration passes (>150 μm) with N_{INP} filter data. All N_{INP} filter results, as well as corresponding N_{INP} results for the days of the clouds passes highlighted with matching color. HVPS data points (with Poisson counting uncertainties) represent maximum N_{ice} concentration observed during the cloud pass, while passes with no ice detected are shown as upper limit error bars to indicate limit of detection (the red bar indicates the limit of detection for the HVPS, i.e., the detection of 1 particle per cloud pass). The N_{INP} parameterization for this study and Cooper 86 range of primary N_{ice} are shown for reference. (b) Example view of rising cloud turret immediately before penetration, taken from forward facing aircraft camera. Red cross illustrates approximate target for cloud penetration.

passes, taken from the aircraft's forward-facing camera, is shown in Figure 9b. We aimed to avoid flying through the same part of a cloud on successive cloud passes to avoid any aircraft influence on our measurements. The nature of the early stages of the development of the convective cloud was that turrets would start to form and dissipate again prior to one turret going on to form the deep convective cloud, hence successive cloud passes in a flight targeted several cloud turrets.

A comparison of the maximum concentration of N_{ice} recorded by the HVPS in each pass, to the N_{INP} spectra measured from the same flight is shown in Figure 9a. For flight C301 on 23rd July, 3 passes were made between −1.3 and −8.0°C (5.4 and 6.5 km ASL respectively) without detecting any ice (<around 0.005 L^{-1}), before the ice was first detected in a pass at −8.2°C (6.5 km). This is consistent with the INP spectra we would have expected to see first ice between about −6 and −10°C. For flight C304, first ice was detected in a pass at −6°C (5.9 km), after two passes warmer than −2°C were made at 5.1 and 5.3 km ASL with no ice detected. Ice was first detected at −6°C, which is again consistent with the INP spectrum. Overall, the temperature at which we first observe ice particles above the detection limit are consistent, within the temperature uncertainties of ∼2°C, to the measured INP spectra.

The N_{ice} on passes at temperature below the temperature at which we observed first ice generally increased with lower temperatures, but in a non-monatonic way. In flight C301, the N_{ice} reached a maximum of 2.5 L^{-1} during the highest altitude pass at −21.5°C (8.7 km), however no ice was detected above the detection limit in a lower pass at −12.3°C (7.4 km). Similarly, the C304 passes showed the N_{ice} increasing non-monotonically with altitude, although all measurements at and below −6°C were above the limit of detection. Overall, the values of N_{ice} in Figure 9 were either within uncertainty of, or lower than, the range of measured N_{INP} for that day. This is consistent with the hypothesis set out above in which we noted that it can take many minutes for ice crystals to grow to 150 μm and this growth rate is slowest around −12 to −8°C (Fuchs et al., 2025; Ryan et al., 1976), where we find the greatest differences between N_{ice} and N_{INP}. Alternatively, the lack of ice may be related to in-homogeneity in the INP concentration related to the fact that the cloud field was very dynamic with turrets forming and subsiding again. If the air sampled in a particular cloud pass had already been involved in a cloud turret some time earlier then it may have already experienced ice formation and precipitation, with the associated removal of those INPs.

21698996, 2026, 3, Downloaded from https://agupubs.onlinelibrary.wiley.com/doi/10.1029/2024JD043236 by University Of Leeds The Brotherton Library, Wiley Online Library on [11/02/2026]. See the Terms and Conditions (https://onlinelibrary.wiley.com/terms-and-conditions) on Wiley Online Library for rules of use; OA articles are governed by the applicable Creative Commons License

21698996, 2026, 3, Downloaded from https://agupubs.onlinelibrary.wiley.com/doi/10.1029/2024JD043236 by University Of Leeds The Brotherton Library, Wiley Online Library on [11/02/2026]. See the Terms and Conditions (https://onlinelibrary.wiley.com/terms-and-conditions) on Wiley Online Library for rules of use; OA articles are governed by the applicable Creative Commons License

The analysis presented in this section is motivating further analysis of aircraft microphysical data from cloud penetration passes from the wider DCMEX flight campaign. This will build on N_{INP} and N_{ice} comparison presented here, using data from particle imaging probes which do not have as high sampling volume as the HVPS (so are less suited to first cloud ice detection) but are capable of resolving ice particles smaller than 150 μm. In conjunction with crystal habit analysis, this will provide further lines of evidence for the primary- and secondary- origin of ice production in young convective turrets in DCMEX. In the future we recommend the use of the new generation of cloud particle imaging probes that maximize both sample volume and resolution in combination with INP measurements to explore the relationship between ice particle production and INP in convective clouds.

4. Concluding Remarks

In conclusion, we have compiled and analyzed an airborne INP data set gathered alongside microphysical data around deep convective clouds in New Mexico. Our data set provides constrained information regarding the temperature range, vertical distribution, and temporal consistency of INPs over a 1-month period during July and August 2022 in the vicinity of deep convective clouds over the Magdalena mountains. We have consistently observed INP within and at the upper range previously reported in continental air and at altitudes extending up to ∼7 km, with no strong linkage to weather or aerosol properties. SEM analysis of filters suggests that, although some primary biological particles were present, the surface area of the coarse mode aerosol collected on the filters is overwhelmingly composed of silicate mineral particles.

The active site density values in Figure 8 are consistent with parameterization for fertile soil dusts where activity is thought to be controlled by the mineral component below about −23°C and a biogenic component at higher temperatures. This is also consistent with the dependencies of the INP concentration spectra on total aerosol concentration shown in Figure 5. Hence, we represent the INP with a two-component model where we use a K-feldspar parameterization to represent the mineral component and an empirical fit to represent the high temperature, probably biogenic, component. This composite curve (Figure B1) results in a "humped" form of INP population, characteristic of the spectra from soil dust that contain appreciable amounts of organic material (O'Sullivan et al., 2018; Suski et al., 2018) and often seen from terrestrial aerosol samples (Testa et al., 2021).

Finally, we compared our INP measurements with near-simultaneous measurements of ice particle number concentration in freshly formed cloud cases from two flights. The temperature at which we first observed ice particles above the instrument detection limit when sequentially flying through rising turrets, was consistent with the measured INP spectra (within about 2°C). At lower temperatures, the ice-particle concentrations were consistent with or smaller than the INP concentrations. We suggest that these results are consistent with primary production being defined by the INP population, but where the growth time scales of ice to detectable sizes (150 μm using the HVPS) meant that in some cloud passes the ice particles had not grown to a detectable size. Future work should focus on the full hydrometeor size distribution, ideally with improved detection limits using high volume, but high-resolution instruments that might detect small concentrations of smaller ice particles. This would provide a more complete picture of ice production and its relationship to the INP population.

Overall, our observations of INP spectra in relationship to ice particle concentrations at the early stages of cloud development, will facilitate the improvement of the representation of convective cloud ice processes in models. Hence, the measurements made in DCMEX and in future campaigns employing a similar design, hopefully with improved instrumentation, will contribute to reducing uncertainty in cloud related climate feedbacks.

Appendix A: Fight and Filter Sampling Run Summary

Below, shown in Table A1, is a full summary of all filter sample runs made during the DCMEX flight campaign, illustrating sampling times, altitudes, volume of air sampled, run mean PCASP aerosol number concentrations and, where available, mineral dust surface area obtained using SEM-EDS.

Table A1
Summary of Filter Sampling Runs

Flight	Date (YYYY-MM-DD)	Filter run	Time start (UTC)	Time end (UTC)	Barometric altitude/ height above ground (m ASL/m AGL)	Total sampled volume PTFE/polycarbonate filter (standard L)	PCASP mean number concentration (cm^{-3} at STP)	SEM- derived mineral dust surface area ($\mu m^2\ cm^{-3}$)	Run type
C297	2022-07-16	C297R1	16:58:28	17:16:20	2.5/0.7	351/141	739	–	Terrain following, HA
		C297R2	17:22:08	17:39:48	2.3/0.5	807/295	722	–	Terrain following, HA
		C297R3	18:01:21	18:18:41	2.5/0.5	330/254	755	–	Terrain following, HA
		C297R4[a]	18:29:49	18:38:14	4.8/3	213/87	590	–	Mid-level, HA
C298	2022-07-19	C298R1	16:40:16	17:07:16	4.8/3	698/-	542	-	Mid-level, HA
		C298R2	17:54:33	18:14:07	2.3/0.5	845/-	397	-	Terrain following, HA
C299	2022-07-20	C299R1	17:15:59	17:36:42	4.8/3	571/-	527	–	Mid-level, HA
		C299R2	17:53:46	18:07:40	2.2/0.4	565/-	431	–	Terrain following, HA
C300	2022-07-22	C300R2	16:39:36	16:51:12	4.8/3	310/121	587	–	Mid-level, HA
		C300R4	17:04:46	17:16:19	2.3/0.4	451/192	495	–	Terrain following, HA
C301	2022-07-23	C301R1	16:10:00	16:27:00	5.1/3.3	425/182	625	–	Mid-level, HA
		C301R2	16:34:00	16:52:00	2.2/0.4	800/343	532	10.2	Terrain following, HA
		C301R3	17:02:00	17:07:00	6/4.2	119/51	615	–	Mid-level, HA
C302	2022-07-24	C302R1	16:23:15	16:41:56	4.6/2.6	438/193	847	5.3	Mid-level, HA
		C302R2	16:45:43	16:49:45	4.5/2.7	114/50	660	–	Mid-level, HA
		C302R3	17:02:12	17:09:45	2.5/0.6	355/162	363	–	Terrain following, HA
		C302R4	17:20:07	17:27:58	2.5/0.5	370/154	498	–	Terrain following, HA
C303	2022-07-25	C303R1	16:04:07	16:18:43	6.5/4.7	235/-	56	–	High alt, LA
		C303R2	16:48:47	17:08:20	4.6/2.8	458/-	536	–	Mid-level, HA
		C303R3	18:15:07	18:33:21	3.5/1.6	777/341	637	–	Mid-level, HA
C304	2022-07-26	C304R1	15:47:49	16:07:37	5.8/4	362/171	115	–	High alt, LA
		C304R2	16:26:47	16:41:46	4.5/2.7	340/147	275	–	Mid-level, HA
		C304R3	18:56:31	19:15:34	2.5/0.7	806/307	488	–	Terrain following, HA
C305	2022-07-27	C305R1	16:53:37	17:12:10	6.5/4.7	285/116	69	–	High alt, LA
		C305R3	19:26:34	19:48:13	3.2/1.4	780/306	522	–	Mid-level, HA
C306	2022-07-29	C306R1	16:12:27	16:30:26	5.4/3.6	411/164	87	–	High alt, LA
		C306R2	17:12:00	17:31:07	2.1/0.3	759/362	808	4.7	Terrain following, HA
C307	2022-07-30	C307R1	16:08:39	16:26:12	6.7/4.9	218/90	45	–	High, low aerosol
		C307R2	17:33:24	17:55:29	2.1/0.3	945/397	601	4.2	Terrain following, HA
		C307R3	18:03:28	18:21:46	2.8/1	729/426	618	–	Mid-level, HA
C308	2022-07-31	C308R1	16:10:35	16:29:59	7.7/5.5	176/78	36	–	High alt, LA
		C308R2	16:40:06	17:01:08	5.1/3.3	498/203	255	–	Mid-level, HA
		C308R3	17:11:41	17:29:04	2.1/0.3	683/341	345	–	Terrain following, HA
C309	2022-08-01	C309R1	16:29:24	16:47:38	6.7/4.9	211/97	35	–	High alt, LA
		C309R2	16:56:23	17:16:18	5.4/3.6	278/270	204	–	Mid-level, HA
		C309R3	17:28:16	17:49:44	2.1/0.3	987/361	610	–	Terrain following, HA
C310	2022-08-02	C310R1	16:00:55	16:22:05	7.1/5.3	166/79	39	–	High alt, LA
		C310R2	16:31:42	16:52:42	4.5/2.7	526/244	395	–	Mid-level, HA
		C310R3	17:03:42	17:20:43	2.1/0.3	774/294	566	–	Terrain following, HA
		C310R4	17:25:49	17:40:25	2/0.1	-/285	557	–	Terrain following, HA
C311	2022-08-03	C311R1	16:06:48	16:26:14	6.5/4.7	247/117	147	–	High alt, LA
		C311R2	16:34:22	16:52:03	5.1/3.3	444/194	444	–	Mid-level, HA

21698996, 2026, 3, Downloaded from https://agupubs.onlinelibrary.wiley.com/doi/10.1029/2024JD043236 by University Of Leeds The Brotherton Library, Wiley Online Library on [11/02/2026]. See the Terms and Conditions (https://onlinelibrary.wiley.com/terms-and-conditions) on Wiley Online Library for rules of use; OA articles are governed by the applicable Creative Commons License

Table A1
Continued

Flight	Date (YYYY-MM-DD)	Filter run	Time start (UTC)	Time end (UTC)	Barometric altitude/ height above ground (m ASL/m AGL)	Total sampled volume PTFE/polycarbonate filter (standard L)	PCASP mean number concentration (cm^{-3} at STP)	SEM- derived mineral dust surface area ($\mu m^2\ cm^{-3}$)	Run type
		C311R3	17:03:46	17:19:26	2.1/0.3	660/295	407	–	Terrain following, HA
		C311R4	17:23:34	17:39:15	1.9/0.1	768/290	388	–	Terrain following, HA
C312	2022-08-04	C312R1	16:40:32	16:58:40	6.5/4.7	306/97	369	–	High alt, HA
		C312R2	17:05:32	17:23:38	4.4/2.6	553/218	803	10.9	Mid-level, HA
		C312R3	17:30:02	17:47:24	2.1/0.3	778/303	400	–	Terrain following, HA
C313	2022-08-06	C313R1	16:02:15	16:21:13	6.5/4.7	-/132	78	–	High alt, LA
		C313R2	16:27:22	16:47:24	4.5/2.7	-/337	550	–	Mid-level, HA
		C313R3	16:54:32	17:12:20	2.1/0.3	-/443	498	–	Terrain following, HA
		C313R4	17:15:47	17:28:12	1.9/0.1	-/203	489	–	Terrain following, HA
C314	2022-08-07	C314R1	16:37:59	16:55:23	6.7/4.9	221/94	25	–	High alt, LA
		C314R2	18:37:09	18:52:30	2.1/0.3	670/288	450	–	Terrain following, HA
C315	2022-08-08	C315R1	16:35:12	16:47:04	4.4/2.6	423/182	363	–	Mid-level, HA

Note. Local time at study site was Mountain Daylight Time (UTC-6). STP = Standard temperature and pressure—298.15 K and 101.325 kPa. HA = High aerosol layer (PCASP N conc >100 cm^{-3}), LA = Low aerosol layer (PCASP N conc <100 cm^{-3}). [a]Run was done over San Mateo Mountain, 30 km SW of Magdalena Mountains.

Appendix B: Parameterization of Ice-Nucleating Particle Concentrations for Cloud Microphysics Models:

In this appendix we parameterize our INP observations primarily so they can be used to predict INP populations in simulations either with clouds sampled during DCMEX or applied to other similar settings dominated by mid-latitude continental aerosol. The comprehensive measurements here provide confidence that INP are consistently present in convection-entrained aerosol during the campaign. Our parametrization $N_{\text{INP-DCMEX}}$ predicts the temperature dependant concentration of INP and is a composite of two components N_{INP1} and N_{INP2}.

N_{INP1} is the component of our INP parameterization that tends to dominate when temperatures <−23°C and is based on an estimate of the mineral dust surface area in combination with the parameterization for K-feldspar from Harrison et al. (2019):

$$N_{\text{INP1}} = A_{\text{dust}} \cdot F_{\text{Ksfp}} \cdot 10^{(n_s(T))} \quad \text{(B1)}$$

where A_{dust} is the mineral dust surface area in $\mu m^2\ cm^{-3}$, F_{Kfsp} is the K-feldspar proportion; $n_s(T)$ is the Harrison et al. (2019) n_s parameterization for K-feldspar, in sites per cm^2 at temperature T in °C ($\log(n_s(T)) = -3.25 + (-0.793\ T) + (-6.91 \times 10^{-2} n\ T^2) + (-4.17 \times 10^{-3}\ T^3) + (-1.05 \times 10^{-4}\ T^4) + (-9.08 \times 10^{-7}\ T^5)$). The mineral surface area used is derived from our SEM-EDS analysis averaged across all samples analyzed ($7.09\ \mu m^2\ cm^{-3}$) and with a K-feldspar proportion of 5% assumed. Examples of this parameterization plotted for individual sample runs with SEM-EDS data available are shown in Section S4 of the Supporting Information S1.

The second component of the parameterization, N_{INP2}, has been fitted to the PTFE filter observations because this study did not establish any physical or environmental parameter that could be used to predict INPs at the higher end of the temperature spectrum. Here, we use a functional form based on that used in Raif et al. (2024), as shown below:

$$N_{\text{INP2}} = a \exp^{(b(T_{\max} - T)^c)} \quad \text{(B2)}$$

where a is a parameter with units of L^{-1}, b and c are dimensionless parameters, T and $T_{\max}$ are the cloud temperature and the temperature of the warmest INP observed respectively, both with units °C. We used filter data

21698996, 2026, 3, Downloaded from https://agupubs.onlinelibrary.wiley.com/doi/10.1029/2024JD043236 by University Of Leeds The Brotherton Library, Wiley Online Library on [11/02/2026]. See the Terms and Conditions (https://onlinelibrary.wiley.com/terms-and-conditions) on Wiley Online Library for rules of use; OA articles are governed by the applicable Creative Commons License

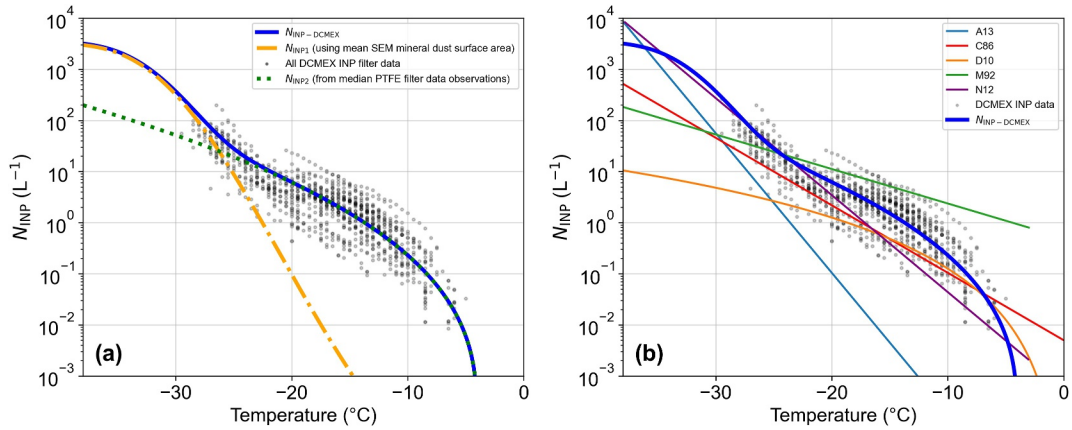

Figure B1. Parameterizations of INP data using the two-component curve, (a) showing the underlying curves for dust and PTFE filter results, (b) in comparison with literature INP parameterizations.

from the High Aerosol layer as these observations are considered most relevant for convection-entrained aerosol and they included relatively few INP data points consistent with background measurements. Using the function fitting package included in the python module SciPy, we obtained fitting parameters according to Equation B2 for every PTFE filter run and then constructed a single representative set of parameters from them. This was done by determining the geometric mean of the INP concentration produced each filters' curve at 2°C intervals, then running the SciPy code again on those points—see Section S4 in Supporting Information S1 for an illustration of this. The final parameters for N_{INP2} are $a = 1.55 \times 10^{-4}$ L^{-1}, $b = 3.734$ and $c = 0.376$. T_{max} was −4°C, implying that at temperatures warmer than this, the INP concentrations tends to zero. Examples of the parameterization plotted for individual sample runs are shown in Section S4 of the Supporting Information S1 and a table of the calculated a, b, and c parameters for each filter are included in the electronic data set.

By summing Equations B1 and B2 applied to the representative mineral dust concentrations and PTFE filter N_{INP} data for the DCMEX campaign respectively, the resulting summed curve, $N_{INP\text{-}DCMEX}$, is shown in Figure B1a and compared with selected existing N_{INP} parameterizations in Figure B1b: A13 (Atkinson et al., 2013), C86 (Cooper, 1986), D10 (DeMott et al., 2010), M92 (Meyers et al., 1992), and N12 (Niemand et al., 2012). This same selection of parametrizations was studied in Hawker, Miltenberger, Wilkinson, et al. (2021), with descriptions of each within this reference. The $N_{INP\text{-}DCMEX}$ curve compares well with C86, although C86 lacks the curvature at warm temperatures. In contrast, D10, which is a prognostic parameterization based on number concentration of aerosol particles >0.5 μm (here we used a value of 0.81 cm^{-3}, the mean value for the High Aerosol layer runs in Table 1), does possess the curvature as seen in our data but produced too low values, owing to the very active fertile dust content observed during this campaign.

Conflict of Interest

The authors declare no conflicts of interest relevant to this study.

Data Availability Statement

The aircraft instrument data used in this publication (aircraft telemetry, PCASP-CDP data, N_{ice} data), is hosted by the Centre for Environmental Data Analysis (CEDA) at https://doi.org/10.5285/B1211AD185E24B488D41DD98F957506C (Facility for Airborne Atmospheric Measurements et al., 2024). A data set containing the filter sampling metadata, INP concentrations (both concentrations and freezing temperatures obtained in the experiments) and SEM-EDS data (size distributions from both SEM and optical probes, as well as EDS size-resolved composition fractions) is available at https://doi.org/10.5518/1815 (Daily et al., 2026). For a comprehensive overview of the wider DCMEX project, including other data sources, we refer the reader to Finney et al. (2024).

21698996, 2026, 3, Downloaded from https://agupubs.onlinelibrary.wiley.com/doi/10.1029/2024JD043236 by University Of Leeds The Brotherton Library, Wiley Online Library on [11/02/2026]. See the Terms and Conditions (https://onlinelibrary.wiley.com/terms-and-conditions) on Wiley Online Library for rules of use; OA articles are governed by the applicable Creative Commons License

Acknowledgments
We thank all the people involved in the DCMEX field campaign, particularly Richard Sonnenfeld of New Mexico Tech for hosting the UK institutions, assisting with the flight campaign planning, providing lightning warnings during flights and facilitating the measurements at the Langmuir Laboratory. Airborne data and samples were obtained using the FAAM Airborne Laboratory BAe-146-301 Atmospheric Research Aircraft (ARA), operated by Airtask Ltd, managed by the National Centre for Atmospheric Science, leased through University of Leeds, and owned by UK Research and Innovation and the Natural Environment Research Council. The FAAM pilots (Steve James, Finbarre Brennan and Mark Robinson) and logistics manager Doug Anderson were central to the success of the campaign. We are also grateful to the staff at the Sheraton Albuquerque Uptown hotel for allowing and facilitating our field analysis. We acknowledge the NCAS Atmospheric Measurement and Observation Facility (AMOF), funded by UKRI–NERC, for providing the HVPS-3 cloud probes. We acknowledge the Centre for Environmental Data Analysis for the access to the FAAM data sets used here, and to Graeme Nott (FAAM) for preparing the CEDA-hosted aircraft instrument data sets. We thank Richard Walshaw at the Leeds Electron Microscopy and Spectroscopy Centre for guidance with the SEM-EDS work. This research has been supported by the Natural Environment Research Council (Grants NE/T014849/1, NE/T006420/1, and NE/T006439/1). Erin N. Raif was supported by the NERC Panorama Doctoral Training Partnership with additional CASE sponsorship from the Met Office (Grant NE/S007458/1).

References

Adebiyi, A., Kok, J. F., Murray, B. J., Ryder, C. L., Stuut, J. B. W., Kahn, R. A., et al. (2023). A review of coarse mineral dust in the Earth system. *Aeolian Research*, *60*, 100849. https://doi.org/10.1016/j.aeolia.2022.100849

Ansmann, A., Tesche, M., Althausen, D., Müller, D., Seifert, P., Freudenthaler, V., et al. (2008). Influence of Saharan dust on cloud glaciation in southern Morocco during the Saharan Mineral Dust Experiment. *Journal of Geophysical Research*, *113*(D4), D04210. https://doi.org/10.1029/2007JD008785

Atkinson, J. D., Murray, B. J., Woodhouse, M. T., Whale, T. F., Baustian, K. J., Carslaw, K. S., et al. (2013). The importance of feldspar for ice nucleation by mineral dust in mixed-phase clouds. *Nature*, *498*(7454), 355–358. https://doi.org/10.1038/nature12278

Barry, K. R., Hill, T. C. J., Levin, E. J. T., Twohy, C. H., Moore, K. A., Weller, Z. D., et al. (2021). Observations of ice nucleating particles in the free troposphere from Western US wildfires. *Journal of Geophysical Research: Atmospheres*, *126*(3), e2020JD033752. https://doi.org/10.1029/2020JD033752

Beall, C. M., Lucero, D., Hill, T. C., DeMott, P. J., Stokes, M. D., & Prather, K. A. (2020). Best practices for precipitation sample storage for offline studies of ice nucleation in marine and coastal environments. *Atmospheric Measurement Techniques*, *13*(12), 6473–6486. https://doi.org/10.5194/amt-13-6473-2020

Beall, C. M., Michaud, J. M., Fish, M. A., Dinasquet, J., Cornwell, G. C., Stokes, M. D., et al. (2021). Cultivable, halotolerant ice nucleating bacteria and fungi in coastal precipitation. *Atmospheric Chemistry and Physics Discussions*, *2021*, 1–33. https://doi.org/10.5194/acp-2020-1229

Blyth, A. M., & Latham, J. (1993). Development of ice and precipitation in New Mexican summertime cumulus clouds. *Quarterly Journal of the Royal Meteorological Society*, *119*(509), 91–120. https://doi.org/10.1002/qj.49711950905

Bogler, S., & Borduas-Dedekind, N. (2020). Lignin's ability to nucleate ice via immersion freezing and its stability towards physicochemical treatments and atmospheric processing. *Atmospheric Chemistry and Physics*, *20*(23), 14509–14522. https://doi.org/10.5194/acp-20-14509-2020

Bony, S., Stevens, B., Coppin, D., Becker, T., Reed, K. A., Voigt, A., & Medeiros, B. (2016). Thermodynamic control of anvil cloud amount. *Proceedings of the National Academy of Sciences of the United States of America*, *113*(32), 8927–8932. https://doi.org/10.1073/pnas.1601472113

Boose, Y., Welti, A., Atkinson, J., Ramelli, F., Danielczok, A., Bingemer, H. G., et al. (2016). Heterogeneous ice nucleation on dust particles sourced from nine deserts worldwide—Part 1: Immersion freezing. *Atmospheric Chemistry and Physics*, *16*(23), 15075–15095. https://doi.org/10.5194/acp-16-15075-2016

Boucher, O., Randall, D., Artaxo, P., Bretherton, C., Feingold, G., Forster, P., et al. (2014). Clouds and aerosols. In *Climate change 2013—The physical science basis: Working group I contribution to the fifth assessment report of the intergovernmental panel on climate change, edited by C. Intergovernmental Panel on Climate* (pp. 571–658). Cambridge University Press. https://doi.org/10.1017/CBO9781107415324.016

Brasseur, Z., Schneider, J., Lampilahti, J., Vakkari, V., Sinclair, V. A., Williamson, C. J., et al. (2024). Vertical distribution of ice nucleating particles over the boreal forest of Hyytiälä, Finland. *Atmospheric Chemistry and Physics*, *24*(19), 11305–11332. https://doi.org/10.5194/acp-24-11305-2024

Cantrell, W., & Heymsfield, A. (2005). Production of ice in tropospheric clouds: A review. *Bulletin of the American Meteorological Society*, *86*(6), 795–808. https://doi.org/10.1175/BAMS-86-6-795

Ceppi, P., Brient, F., Zelinka, M. D., & Hartmann, D. L. (2017). Cloud feedback mechanisms and their representation in global climate models. *WIREs Climate Change*, *8*(4), e465. https://doi.org/10.1002/wcc.465

Cochet, N., & Widehem, P. (2000). Ice crystallization by Pseudomonas syringae. *Applied Microbiology and Biotechnology*, *54*(2), 153–161. https://doi.org/10.1007/s002530000377

Conen, F., Morris, C. E., Leifeld, J., Yakutin, M. V., & Alewell, C. (2011). Biological residues define the ice nucleation properties of soil dust. *Atmospheric Chemistry and Physics*, *11*(18), 9643–9648. https://doi.org/10.5194/acp-11-9643-2011

Conen, F., & Yakutin, M. V. (2018). Soils rich in biological ice-nucleating particles abound in ice-nucleating macromolecules likely produced by fungi. *Biogeosciences*, *15*(14), 4381–4385. https://doi.org/10.5194/bg-15-4381-2018

Cooper, W. A. (1986). Ice initiation in natural clouds. In R. R. Braham, et al. (Eds.), *Precipitation enhancement—A scientific challenge* (pp. 29–32). American Meteorological Society. https://doi.org/10.1007/978-1-935704-17-1_4

Creamean, J. M., Suski, K. J., Rosenfeld, D., Cazorla, A., DeMott, P. J., Sullivan, R. C., et al. (2013). Dust and biological aerosols from the Sahara and Asia influence precipitation in the Western U.S. *Science*, *339*(6127), 1572–1578. https://doi.org/10.1126/science.1227279

Crosier, J., Bower, K. N., Choularton, T. W., Westbrook, C. D., Connolly, P. J., Cui, Z. Q., et al. (2011). Observations of ice multiplication in a weakly convective cell embedded in supercooled mid-level stratus. *Atmospheric Chemistry and Physics*, *11*(1), 257–273. https://doi.org/10.5194/acp-11-257-2011

Daily, M. I., Robinson, J., Finney, D., Raif, E., McQuaid, J. B., Hu, K., et al. (2026). Dataset associated with "Ice-nucleating particle and cloud ice crystal concentrations associated with developing summertime deep convective clouds in south-western USA" by Daily et al, 2026 [Dataset]. *University of Leeds*. https://doi.org/10.5518/1815

Daily, M. I., Tarn, M. D., Whale, T. F., & Murray, B. J. (2022). An evaluation of the heat test for the ice-nucleating ability of minerals and biological material. *Atmospheric Measurement Techniques*, *15*(8), 2635–2665. https://doi.org/10.5194/amt-15-2635-2022

DeMott, P. J., Prenni, A. J., Liu, X., Kreidenweis, S. M., Petters, M. D., Twohy, C. H., et al. (2010). Predicting global atmospheric ice nuclei distributions and their impacts on climate. *Proceedings of the National Academy of Sciences of the United States of America*, *107*(25), 11217–11222. https://doi.org/10.1073/pnas.0910818107

DeMott, P. J., Prenni, A. J., McMeeking, G. R., Sullivan, R. C., Petters, M. D., Tobo, Y., et al. (2015). Integrating laboratory and field data to quantify the immersion freezing ice nucleation activity of mineral dust particles. *Atmospheric Chemistry and Physics*, *15*(1), 393–409. https://doi.org/10.5194/acp-15-393-2015

Deng, X., Xue, H., & Meng, Z. (2018). The effect of ice nuclei on a deep convective cloud in South China. *Atmospheric Research*, *206*, 1–12. https://doi.org/10.1016/j.atmosres.2018.02.013

Dreischmeier, K., Budke, C., Wiehemeier, L., Kottke, T., & Koop, T. (2017). Boreal pollen contain ice-nucleating as well as ice-binding "antifreeze" polysaccharides. *Scientific Reports*, *7*(1), 41890. https://doi.org/10.1038/srep41890

Facility for Airborne Atmospheric Measurements, et al. (2024). DCMEX: Collection of in-situ airborne observations, ground-based meteorological and aerosol measurements and cloud imagery for the Deep Convective Microphysics Experiment [Dataset]. *NERC EDS Centre for Environmental Data Analysis*. https://doi.org/10.5285/B1211AD185E24B488D41DD98F957506C

Fan, J., Comstock, J. M., & Ovchinnikov, M. (2010). The cloud condensation nuclei and ice nuclei effects on tropical anvil characteristics and water vapor of the tropical tropopause layer. *Environmental Research Letters*, *5*(4), 044005. https://doi.org/10.1088/1748-9326/5/4/044005

21698996, 2026, 3, Downloaded from https://agupubs.onlinelibrary.wiley.com/doi/10.1029/2024JD043236 by University Of Leeds The Brotherton Library, Wiley Online Library on [11/02/2026]. See the Terms and Conditions (https://onlinelibrary.wiley.com/terms-and-conditions) on Wiley Online Library for rules of use; OA articles are governed by the applicable Creative Commons License

Fan, J., Leung, L. R., Rosenfeld, D., & DeMott, P. J. (2017). Effects of cloud condensation nuclei and ice nucleating particles on precipitation processes and supercooled liquid in mixed-phase orographic clouds. *Atmospheric Chemistry and Physics*, *17*(2), 1017–1035. https://doi.org/10.5194/acp-17-1017-2017

Field, P. R., Lawson, R. P., Brown, P. R. A., Lloyd, G., Westbrook, C., Moisseev, D., et al. (2017). Secondary ice production: Current state of the science and recommendations for the future. *Meteorological Monographs*, *58*(7), 1–7.20. https://doi.org/10.1175/AMSMONOGRAPHS-D-16-0014.1

Field, P. R., Heymsfield, A. J., Shipway, B. J., DeMott, P. J., Pratt, K. A., Rogers, D. C., et al. (2012). Ice in clouds experiment–layer clouds. Part II: Testing characteristics of heterogeneous ice formation in lee wave clouds. *Journal of the Atmospheric Sciences*, *69*(3), 1066–1079. https://doi.org/10.1175/JAS-D-11-026.1

Finney, D. L., Blyth, A. M., Gallagher, M., Wu, H., Nott, G. J., Biggerstaff, M. I., et al. (2024). Deep Convective Microphysics Experiment (DCMEX) coordinated aircraft and ground observations: Microphysics, aerosol, and dynamics during cumulonimbus development. *Earth System Science Data*, *16*(5), 2141–2163. https://doi.org/10.5194/essd-16-2141-2024

Fletcher, N., Squires, P., & Bowen, E. (1962). *The physics of rainclouds*. Cambridge University Press. https://doi.org/10.1002/qj.49708837821

Fuchs, C., Ramelli, F., Miller, A. J., Omanovic, N., Spirig, R., Zhang, H., et al. (2025). Quantifying ice crystal growth rates in natural clouds from glaciogenic cloud seeding experiments. *Atmospheric Chemistry and Physics*, *25*(19), 12177–12196. https://doi.org/10.5194/acp-25-12177-2025

Garcia, E., Hill, T. C. J., Prenni, A. J., DeMott, P. J., Franc, G. D., & Kreidenweis, S. M. (2012). Biogenic ice nuclei in boundary layer air over two U.S. High Plains agricultural regions. *Journal of Geophysical Research*, *117*(D18). https://doi.org/10.1029/2012jd018343

Gettelman, A., & Sherwood, S. C. (2016). Processes responsible for cloud feedback. *Current Climate Change Reports*, *2*(4), 179–189. https://doi.org/10.1007/s40641-016-0052-8

Gibbons, M., Min, Q., & Fan, J. (2018). Investigating the impacts of Saharan dust on tropical deep convection using spectral bin microphysics. *Atmospheric Chemistry and Physics*, *18*(16), 12161–12184. https://doi.org/10.5194/acp-18-12161-2018

Hader, J. D., Wright, T. P., & Petters, M. D. (2014). Contribution of pollen to atmospheric ice nuclei concentrations. *Atmospheric Chemistry and Physics*, *14*(11), 5433–5449. https://doi.org/10.5194/acp-14-5433-2014

Hallett, J., & Mossop, S. C. (1974). Production of secondary ice particles during the riming process. *Nature*, *249*(5452), 26–28. https://doi.org/10.1038/249026a0

Harrison, A. D., Lever, K., Sanchez-Marroquin, A., Holden, M. A., Whale, T. F., Tarn, M. D., et al. (2019). The ice-nucleating ability of quartz immersed in water and its atmospheric importance compared to K-feldspar. *Atmospheric Chemistry and Physics*, *19*(17), 11343–11361. https://doi.org/10.5194/acp-19-11343-2019

Harrison, A. D., O'Sullivan, D., Adams, M. P., Porter, G. C. E., Blades, E., Brathwaite, C., et al. (2022). The ice-nucleating activity of African mineral dust in the Caribbean boundary layer. *Atmospheric Chemistry and Physics*, *22*(14), 9663–9680. https://doi.org/10.5194/acp-22-9663-2022

Harrison, A. D., Whale, T. F., Carpenter, M. A., Holden, M. A., Neve, L., O'Sullivan, D., et al. (2016). Not all feldspars are equal: A survey of ice nucleating properties across the feldspar group of minerals. *Atmospheric Chemistry and Physics*, *16*(17), 10927–10940. https://doi.org/10.5194/acp-16-10927-2016

Hartmann, D. L., Gasparini, B., Berry, S. E., & Blossey, P. N. (2018). The life cycle and net radiative effect of tropical anvil clouds. *Journal of Advances in Modeling Earth Systems*, *10*(12), 3012–3029. https://doi.org/10.1029/2018MS001484

Hawker, R. E., Miltenberger, A. K., Johnson, J. S., Wilkinson, J. M., Hill, A. A., Shipway, B. J., et al. (2021). Model emulation to understand the joint effects of ice-nucleating particles and secondary ice production on deep convective anvil cirrus. *Atmospheric Chemistry and Physics*, *21*(23), 17315–17343. https://doi.org/10.5194/acp-21-17315-2021

Hawker, R. E., Miltenberger, A. K., Wilkinson, J. M., Hill, A. A., Shipway, B. J., Cui, Z., et al. (2021). The temperature dependence of ice-nucleating particle concentrations affects the radiative properties of tropical convective cloud systems. *Atmospheric Chemistry and Physics*, *21*(7), 5439–5461. https://doi.org/10.5194/acp-21-5439-2021

He, C., Yin, Y., Huang, Y., Kuang, X., Cui, Y., Chen, K., et al. (2023). The vertical distribution of ice-nucleating particles over the North China Plain: A case of cold front passage. *Remote Sensing*, *15*(20), 4989. https://doi.org/10.3390/rs15204989

Herbert, R. J., Murray, B. J., Dobbie, S. J., & Koop, T. (2015). Sensitivity of liquid clouds to homogenous freezing parameterizations. *Geophysical Research Letters*, *42*(5), 1599–1605. https://doi.org/10.1002/2014GL062729

Herbert, R. J., Sanchez-Marroquin, A., Grosvenor, D. P., Pringle, K. J., Arnold, S. R., Murray, B. J., & Carslaw, K. S. (2025). Gaps in our understanding of ice-nucleating particle sources exposed by global simulation of the UK Earth System Model. *Atmospheric Chemistry and Physics*, *25*(1), 291–325. https://doi.org/10.5194/acp-25-291-2025

Hill, T. C. J., Moffett, B. F., Demott, P. J., Georgakopoulos, D. G., Stump, W. L., & Franc, G. D. (2014). Measurement of ice nucleation-active bacteria on plants and in precipitation by quantitative PCR. *Applied and Environmental Microbiology*, *80*(4), 1256–1267. https://doi.org/10.1128/AEM.02967-13

Hiranuma, N., Adachi, K., Bell, D. M., Belosi, F., Beydoun, H., Bhaduri, B., et al. (2019). A comprehensive characterization of ice nucleation by three different types of cellulose particles immersed in water. *Atmospheric Chemistry and Physics*, *19*(7), 4823–4849. https://doi.org/10.5194/acp-19-4823-2019

Hiranuma, N., Auvermann, B. W., Belosi, F., Bush, J., Cory, K. M., Georgakopoulos, D. G., et al. (2021). Laboratory and field studies of ice-nucleating particles from open-lot livestock facilities in Texas. *Atmospheric Chemistry and Physics*, *21*(18), 14215–14234. https://doi.org/10.5194/acp-21-14215-2021

Hobbs, P. V., & Rangno, A. L. (1985). Ice particle concentrations in clouds. *Journal of the Atmospheric Sciences*, *42*(23), 2523–2549. https://doi.org/10.1175/1520-0469(1985)042<2523:IPCIC>2.0.CO;2

Hoffmann, F., Raasch, S., & Noh, Y. (2015). Entrainment of aerosols and their activation in a shallow cumulus cloud studied with a coupled LCM–LES approach. *Atmospheric Research*, *156*, 43–57. https://doi.org/10.1016/j.atmosres.2014.12.008

Huang, S., Hu, W., Chen, J., Wu, Z., Zhang, D., & Fu, P. (2021). Overview of biological ice nucleating particles in the atmosphere. *Environment International*, *146*, 106197. https://doi.org/10.1016/j.envint.2020.106197

Ickes, L., Welti, A., Hoose, C., & Lohmann, U. (2015). Classical nucleation theory of homogeneous freezing of water: Thermodynamic and kinetic parameters. *Physical Chemistry Chemical Physics*, *17*(8), 5514–5537. https://doi.org/10.1039/C4CP04184D

Kanji, Z. A., Ladino, L. A., Wex, H., Boose, Y., Burkert-Kohn, M., Cziczo, D. J., & Krämer, M. (2017). Overview of ice nucleating particles. *Meteorological Monographs*, *58*, 1.1–1.33. https://doi.org/10.1175/AMSMONOGRAPHS-D-16-0006.1

Knopf, D. A., Wang, P., Wong, B., Tomlin, J. M., Veghte, D. P., Lata, N. N., et al. (2023). Physicochemical characterization of free troposphere and marine boundary layer ice-nucleating particles collected by aircraft in the eastern North Atlantic. *Atmospheric Chemistry and Physics*, *23*(15), 8659–8681. https://doi.org/10.5194/acp-23-8659-2023

21698996, 2026, 3, Downloaded from https://agupubs.onlinelibrary.wiley.com/doi/10.1029/2024JD043236 by University Of Leeds The Brotherton Library, Wiley Online Library on [11/02/2026]. See the Terms and Conditions (https://onlinelibrary.wiley.com/terms-and-conditions) on Wiley Online Library for rules of use; OA articles are governed by the applicable Creative Commons License

Korolev, A., & Leisner, T. (2020). Review of experimental studies of secondary ice production. *Atmospheric Chemistry and Physics*, *20*(20), 11767–11797. https://doi.org/10.5194/acp-20-11767-2020

Lawson, R. P., Korolev, A. V., DeMott, P. J., Heymsfield, A. J., Bruintjes, R. T., Wolff, C. A., et al. (2023). The Secondary Production of Ice in Cumulus Experiment (SPICULE). *Bulletin of the American Meteorological Society*, *104*(1), E51–E76. https://doi.org/10.1175/BAMS-D-21-0209.1

Lawson, R. P., O'Connor, D., Zmarzly, P., Weaver, K., Baker, B., Mo, Q., & Jonsson, H. (2006). The 2D-S (Stereo) probe: Design and preliminary tests of a new airborne, high-speed, high-resolution particle imaging probe. *Journal of Atmospheric and Oceanic Technology*, *23*(11), 1462–1477. https://doi.org/10.1175/JTECH1927.1

Levin, E. J. T., DeMott, P. J., Suski, K. J., Boose, Y., Hill, T. C., McCluskey, C. S., et al. (2019). Characteristics of ice nucleating particles in and around California winter storms. *Journal of Geophysical Research: Atmospheres*, *124*(21), 11530–11551. https://doi.org/10.1029/2019JD030831

Lloyd, G., Choularton, T., Bower, K., Crosier, J., Gallagher, M., Flynn, M., et al. (2020). Small ice particles at slightly supercooled temperatures in tropical maritime convection. *Atmospheric Chemistry and Physics*, *20*(6), 3895–3904. https://doi.org/10.5194/acp-20-3895-2020

Maki, L. R., Galyan, E. L., Chang-Chien, M. M., & Caldwell, D. R. (1974). Ice nucleation induced by pseudomonas syringae. *Applied Microbiology*, *28*(3), 456–459. https://doi.org/10.1128/am.28.3.456-459.1974

Matthews, B. H., Alsante, A. N., & Brooks, S. D. (2023). Pollen emissions of subpollen particles and ice nucleating particles. *ACS Earth and Space Chemistry*, *7*(6), 1207–1218. https://doi.org/10.1021/acsearthspacechem.3c00014

McCluskey, C. S., Ovadnevaite, J., Rinaldi, M., Atkinson, J., Belosi, F., Ceburnis, D., et al. (2018). Marine and terrestrial organic ice-nucleating particles in pristine marine to continentally influenced northeast Atlantic air masses. *Journal of Geophysical Research: Atmospheres*, *123*(11), 6196–6212. https://doi.org/10.1029/2017JD028033

McFarquhar, G. M., Baumgardner, D., & Heymsfield, A. J. (2017). Ice formation and evaluation in clouds and precipitation. *Meteorological Monographs*, *58*(1), v–ix. https://doi.org/10.1175/AMSMONOGRAPHS-D-16-0018.1

Meyers, M. P., DeMott, P. J., & Cotton, W. R. (1992). New primary ice-nucleation parameterizations in an explicit cloud model. *Journal of Applied Meteorology and Climatology*, *31*(7), 708–721. https://doi.org/10.1175/1520-0450(1992)031<0708:NPINPI>2.0.CO;2

Moore, K. A., Hill, T. C. J., McCluskey, C. S., Twohy, C. H., Rainwater, B., Toohey, D. W., et al. (2024). Characterizing ice nucleating particles over the Southern Ocean using simultaneous aircraft and ship observations. *Journal of Geophysical Research: Atmospheres*, *129*(2), e2023JD039543. https://doi.org/10.1029/2023JD039543

Morris, C. E., Sands, D. C., Glaux, C., Samsatly, J., Asaad, S., Moukahel, A. R., et al. (2013). Urediospores of rust fungi are ice nucleation active at > -10°C and harbor ice nucleation active bacteria. *Atmospheric Chemistry and Physics*, *13*(8), 4223–4233. https://doi.org/10.5194/acp-13-4223-2013

Mossop, S. C., & Ono, A. (1969). Measurements of ice crystal concentration in clouds. *Journal of the Atmospheric Sciences*, *26*(1), 130–137. https://doi.org/10.1175/1520-0469(1969)026<0130:MOICCI>2.0.CO;2

Murray, B. J., O'Sullivan, D., Atkinson, J. D., & Webb, M. E. (2012). Ice nucleation by particles immersed in supercooled cloud droplets. *Chemical Society Reviews*, *41*(19), 6519–6554. https://doi.org/10.1039/C2CS35200A

Murray, K. A., Kinney, N. L. H., Griffiths, C. A., Hasan, M., Gibson, M. I., & Whale, T. F. (2022). Pollen derived macromolecules serve as a new class of ice-nucleating cryoprotectants. *Scientific Reports*, *12*(1), 12295. https://doi.org/10.1038/s41598-022-15545-4

Niemand, M., Möhler, O., Vogel, B., Vogel, H., Hoose, C., Connolly, P., et al. (2012). A particle-surface-area-based parameterization of immersion freezing on desert dust particles. *Journal of the Atmospheric Sciences*, *69*(10), 3077–3092. https://doi.org/10.1175/JAS-D-11-0249.1

O'Sullivan, D., Adams, M. P., Tarn, M. D., Harrison, A. D., Vergara-Temprado, J., Porter, G. C. E., et al. (2018). Contributions of biogenic material to the atmospheric ice-nucleating particle population in North Western Europe. *Scientific Reports*, *8*(1), 13821. https://doi.org/10.1038/s41598-018-31981-7

O'Sullivan, D., Murray, B. J., Malkin, T. L., Whale, T. F., Umo, N. S., Atkinson, J. D., et al. (2014). Ice nucleation by fertile soil dusts: Relative importance of mineral and biogenic components. *Atmospheric Chemistry and Physics*, *14*(4), 1853–1867. https://doi.org/10.5194/acp-14-1853-2014

O'Sullivan, D., Murray, B. J., Ross, J. F., & Webb, M. E. (2016). The adsorption of fungal ice-nucleating proteins on mineral dusts: A terrestrial reservoir of atmospheric ice-nucleating particles. *Atmospheric Chemistry and Physics*, *16*(12), 7879–7887. https://doi.org/10.5194/acp-16-7879-2016

O'Sullivan, D., Murray, B. J., Ross, J. F., Whale, T. F., Price, H. C., Atkinson, J. D., et al. (2015). The relevance of nanoscale biological fragments for ice nucleation in clouds. *Scientific Reports*, *5*(1), 8082. https://doi.org/10.1038/srep08082

Patade, S., Nagare, B., Wagh, S., Maheskumar, R. S., Prabha, T. V., & Pradeep Kumar, P. (2014). Deposition ice nuclei observations over the Indian region during CAIPEEX. *Atmospheric Research*, *149*, 300–314. https://doi.org/10.1016/j.atmosres.2014.07.001

Patnaude, R. J., McCluskey, C. S., Roberts, G. C., DeMott, P. J., Hill, T. C. J., McFarquhar, G. M., et al. (2025). Characteristics of ice nucleating particles from the long-range transport of Saharan dust. *Geophysical Research Letters*, *52*(11), e2024GL113365. https://doi.org/10.1029/2024GL113365

Petters, M. D., & Wright, T. P. (2015). Revisiting ice nucleation from precipitation samples. *Geophysical Research Letters*, *42*(20), 8758–8766. https://doi.org/10.1002/2015GL065733

Price, H. C., Baustian, K. J., McQuaid, J. B., Blyth, A., Bower, K. N., Choularton, T., et al. (2018). Atmospheric ice-nucleating particles in the dusty tropical Atlantic. *Journal of Geophysical Research: Atmospheres*, *123*(4), 2175–2193. https://doi.org/10.1002/2017JD027560

Pummer, B. G., Bauer, H., Bernardi, J., Bleicher, S., & Grothe, H. (2012). Suspendable macromolecules are responsible for ice nucleation activity of birch and conifer pollen. *Atmospheric Chemistry and Physics*, *12*(5), 2541–2550. https://doi.org/10.5194/acp-12-2541-2012

Raif, E. N., Barr, S. L., Tarn, M. D., McQuaid, J. B., Daily, M. I., Abel, S. J., et al. (2024). High ice-nucleating particle concentrations associated with Arctic haze in springtime cold-air outbreaks. *Atmospheric Chemistry and Physics*, *24*(24), 14045–14072. https://doi.org/10.5194/acp-24-14045-2024

Rosenberg, P. D., Dean, A. R., Williams, P. I., Dorsey, J. R., Minikin, A., Pickering, M. A., & Petzold, A. (2012). Particle sizing calibration with refractive index correction for light scattering optical particle counters and impacts upon PCASP and CDP data collected during the Fennec campaign. *Atmospheric Measurement Techniques*, *5*(5), 1147–1163. https://doi.org/10.5194/amt-5-1147-2012

Ryan, B. F., Wishart, E. R., & Shaw, D. E. (1976). The growth rates and densities of ice crystals between -3°C and -21°C. *Journal of the Atmospheric Sciences*, *33*(5), 842–850. https://doi.org/10.1175/1520-0469(1976)033<0842:tgrado>2.0.co;2

Sanchez-Marroquin, A., Arnalds, O., Baustian-Dorsi, K. J., Browse, J., Dagsson-Waldhauserova, P., Harrison, A. D., et al. (2020). Iceland is an episodic source of atmospheric ice-nucleating particles relevant for mixed-phase clouds. *Science Advances*, *6*(26), eaba8137. https://doi.org/10.1126/sciadv.aba8137

21698996, 2026, 3, Downloaded from https://agupubs.onlinelibrary.wiley.com/doi/10.1029/2024JD043236 by University Of Leeds The Brotherton Library, Wiley Online Library on [11/02/2026]. See the Terms and Conditions (https://onlinelibrary.wiley.com/terms-and-conditions) on Wiley Online Library for rules of use; OA articles are governed by the applicable Creative Commons License

Sanchez-Marroquin, A., Barr, S. L., Burke, I. T., McQuaid, J. B., & Murray, B. J. (2023). Aircraft ice-nucleating particle and aerosol composition measurements in the western North American Arctic. *Atmospheric Chemistry and Physics*, *23*(21), 13819–13834. https://doi.org/10.5194/acp-23-13819-2023

Sanchez-Marroquin, A., Hedges, D. H. P., Hiscock, M., Parker, S. T., Rosenberg, P. D., Trembath, J., et al. (2019). Characterisation of the filter inlet system on the FAAM BAe-146 research aircraft and its use for size-resolved aerosol composition measurements. *Atmospheric Measurement Techniques*, *12*(11), 5741–5763. https://doi.org/10.5194/amt-12-5741-2019

Sanchez-Marroquin, A., West, J. S., Burke, I. T., McQuaid, J. B., & Murray, B. J. (2021). Mineral and biological ice-nucleating particles above the South East of the British Isles. *Environmental Science: Atmospheres*, *1*(4), 176–191. https://doi.org/10.1039/D1EA00003A

Schnell, R. C. (1982). Airborne ice nucleus measurements around the Hawaiian Islands. *Journal of Geophysical Research*, *87*(C11), 8886–8890. https://doi.org/10.1029/JC087iC11p08886

Sherwood, S. C., Webb, M. J., Annan, J. D., Armour, K. C., Forster, P. M., Hargreaves, J. C., et al. (2020). An assessment of earth's climate sensitivity using multiple lines of evidence. *Reviews of Geophysics*, *58*(4), e2019RG000678. https://doi.org/10.1029/2019RG000678

Spracklen, D. V., & Heald, C. L. (2014). The contribution of fungal spores and bacteria to regional and global aerosol number and ice nucleation immersion freezing rates. *Atmospheric Chemistry and Physics*, *14*(17), 9051–9059. https://doi.org/10.5194/acp-14-9051-2014

Steinke, I., Funk, R., Busse, J., Iturri, A., Kirchen, S., Leue, M., et al. (2016). Ice nucleation activity of agricultural soil dust aerosols from Mongolia, Argentina, and Germany. *Journal of Geophysical Research: Atmospheres*, *121*(22), 13559–13576. https://doi.org/10.1002/2016JD025160

Suski, K. J., Hill, T. C. J., Levin, E. J. T., Miller, A., DeMott, P. J., & Kreidenweis, S. M. (2018). Agricultural harvesting emissions of ice-nucleating particles. *Atmospheric Chemistry and Physics*, *18*(18), 13755–13771. https://doi.org/10.5194/acp-18-13755-2018

Taylor, J. W., Choularton, T. W., Blyth, A. M., Liu, Z., Bower, K. N., Crosier, J., et al. (2016). Observations of cloud microphysics and ice formation during COPE. *Atmospheric Chemistry and Physics*, *16*(2), 799–826. https://doi.org/10.5194/acp-16-799-2016

Testa, B., Hill, T. C. J., Marsden, N. A., Barry, K. R., Hume, C. C., Bian, Q., et al. (2021). Ice nucleating particle connections to regional Argentinian land surface emissions and weather during the cloud, aerosol, and complex terrain interactions experiment. *Journal of Geophysical Research: Atmospheres*, *126*(23), e2021JD035186. https://doi.org/10.1029/2021JD035186

Tobo, Y., DeMott, P. J., Hill, T. C. J., Prenni, A. J., Swoboda-Colberg, N. G., Franc, G. D., & Kreidenweis, S. M. (2014). Organic matter matters for ice nuclei of agricultural soil origin. *Atmospheric Chemistry and Physics*, *14*(16), 8521–8531. https://doi.org/10.5194/acp-14-8521-2014

Tobo, Y., Prenni, A. J., DeMott, P. J., Huffman, J. A., McCluskey, C. S., Tian, G., et al. (2013). Biological aerosol particles as a key determinant of ice nuclei populations in a forest ecosystem. *Journal of Geophysical Research: Atmospheres*, *118*(17), 10100–10110. https://doi.org/10.1002/jgrd.50801

Vali, G. (1971). Quantitative evaluation of experimental results an the heterogeneous freezing nucleation of supercooled liquids. *Journal of the Atmospheric Sciences*, *28*(3), 402–409. https://doi.org/10.1175/1520-0469(1971)028<0402:qeoera>2.0.co;2

Vali, G. (2019). Revisiting the differential freezing nucleus spectra derived from drop-freezing experiments: Methods of calculation, applications, and confidence limits. *Atmospheric Measurement Techniques*, *12*(2), 1219–1231. https://doi.org/10.5194/amt-12-1219-2019

Vali, G., DeMott, P. J., Möhler, O., & Whale, T. F. (2015). Technical note: A proposal for ice nucleation terminology. *Atmospheric Chemistry and Physics*, *15*(18), 10263–10270. https://doi.org/10.5194/acp-15-10263-2015

Vergara-Temprado, J., Murray, B. J., Wilson, T. W., O'Sullivan, D., Browse, J., Pringle, K. J., et al. (2017). Contribution of feldspar and marine organic aerosols to global ice nucleating particle concentrations. *Atmospheric Chemistry and Physics*, *17*(5), 3637–3658. https://doi.org/10.5194/acp-17-3637-2017

Whale, T. F., Murray, B. J., O'Sullivan, D., Wilson, T. W., Umo, N. S., Baustian, K. J., et al. (2015). A technique for quantifying heterogeneous ice nucleation in microlitre supercooled water droplets. *Atmospheric Measurement Techniques*, *8*(6), 2437–2447. https://doi.org/10.5194/amt-8-2437-2015

Wilbourn, E. K., Lacher, L., Guerrero, C., Vepuri, H. S. K., Höhler, K., Nadolny, J., et al. (2024). Measurement report: A comparison of ground-level ice-nucleating-particle abundance and aerosol properties during autumn at contrasting marine and terrestrial locations. *Atmospheric Chemistry and Physics*, *24*(9), 5433–5456. https://doi.org/10.5194/acp-24-5433-2024

Wilson, T. W., Ladino, L. A., Alpert, P. A., Breckels, M. N., Brooks, I. M., Browse, J., et al. (2015). A marine biogenic source of atmospheric ice-nucleating particles. *Nature*, *525*(7568), 234–238. https://doi.org/10.1038/nature14986

Wu, J., Yin, Y., Chen, K., He, C., Jiang, H., Zheng, B., et al. (2022). Vertical distribution of atmospheric ice nucleating particles in winter over northwest China based on aircraft observations. *Atmosphere*, *13*(9), 1447. https://doi.org/10.3390/atmos13091447

Yang, J., Wang, Z., Heymsfield, A. J., DeMott, P. J., Twohy, C. H., Suski, K. J., & Toohey, D. W. (2020). High ice concentration observed in tropical maritime stratiform mixed-phase clouds with top temperatures warmer than −8°C. *Atmospheric Research*, *233*, 104719. https://doi.org/10.1016/j.atmosres.2019.104719

Zaremba, T. J., Rauber, R. M., McFarquhar, G. M., DeMott, P. J., D'Alessandro, J. J., & Wu, W. (2021). Ice in Southern Ocean clouds with cloud top temperatures exceeding −5°C. *Journal of Geophysical Research: Atmospheres*, *126*(14), e2021JD034574. https://doi.org/10.1029/2021JD034574

21698996, 2026, 3, Downloaded from https://agupubs.onlinelibrary.wiley.com/doi/10.1029/2024JD043236 by University Of Leeds The Brotherton Library, Wiley Online Library on [11/02/2026]. See the Terms and Conditions (https://onlinelibrary.wiley.com/terms-and-conditions) on Wiley Online Library for rules of use; OA articles are governed by the applicable Creative Commons License